

FARADAY CONVERSION IN TURBULENT BLAZAR JETS

NICHOLAS R. MACDONALD AND ALAN P. MARSCHER

Institute for Astrophysical Research, Boston University, 725 Commonwealth Avenue, Boston, MA 02215
Draft version January 19, 2023

ABSTRACT

Low ($\lesssim 3\%$) levels of circular polarization (CP) detected at radio frequencies in the relativistic jets of some blazars can provide insight into the underlying nature of the jet plasma. CP can be produced through linear birefringence, in which initially linearly polarized emission produced in one region of the jet is altered by Faraday rotation as it propagates through other regions of the jet with various magnetic field orientations. Marscher has recently begun a study of jets with such magnetic geometries with the Turbulent Extreme Multi-Zone (TEMZ) model, in which turbulent plasma crossing a standing shock in the jet is represented by a collection of thousands of individual plasma cells, each with distinct magnetic field orientation. Here we develop a radiative transfer scheme that allows the numerical TEMZ code to produce simulated images of the time-dependent linearly and circularly polarized intensity at different radio frequencies. In this initial study, we produce synthetic polarized emission maps that highlight the linear and circular polarization expected within the model.

Subject headings: blazars: non-thermal radiative transfer - relativistic processes - polarization

1. INTRODUCTION

Observations of the polarization of synchrotron radio emission from the jets of blazars provide a probe of the underlying magnetic field structure that is thought to play an important role in the dynamics of these highly relativistic flows. Low levels of circularly polarized intensity (Stokes V) have been detected in a number of blazar jets (Wardle et al. 1998; Homan & Wardle 1999; Homan et al. 2009). While typically $<0.5\%$ of the total intensity (Stokes I), circular polarization (CP) can give us insight into the underlying nature of the jet plasma (Wardle et al. 1998). Unlike linear polarization (LP), which can be altered by Faraday rotation in magnetized plasma both within and external to the jet, CP is produced at levels $<1\%$ by the basic synchrotron process, or at potentially higher levels through Faraday conversion from LP to CP as the radiation propagates through the jet. A measurement of the fractional CP ($m_c \equiv -V/I$) emanating from the jet can probe the charge asymmetry of leptons within the jet plasma, and therefore the ratio of the number of positrons to protons (Wardle et al. 1998; Ruszkowski & Begelman 2002; Homan et al. 2009).

LP from blazars at high radio frequencies ranges from several percent or less to tens of percent, with the higher values tending to occur downstream of the most compact emission (the “core”) seen on very long baseline interferometry (VLBI) images (e.g., Cawthorne et al. 1993; Marscher et al. 2002). The LP of blazars at optical wavelengths (e.g., Smith 2016) and in the millimeter-wave core (Jorstad et al. 2007) is both variable and weaker than the 70-75% value from synchrotron emission in a uniform magnetic field, characteristics that can be explained through turbulent disordering of the field. Motivated by such observations, Marscher (2014) has developed the Turbulent Extreme Multi-Zone (TEMZ) model for blazar emission. The TEMZ model consists of thousands of individual cells of plasma that propagate relativistically across a standing shock in the jet (Figure 1). Each cell of plasma within the model contains a distinct

magnetic field that combines a turbulent component with an underlying ordered component. The aggregate of the emission from these cells is able to reproduce (in a statistical sense) the LP that is typically seen in blazars, including the observed level of variability in both degree and position angle (Marscher 2015). The turbulent nature of the magnetic field within the TEMZ grid naturally creates a birefringent environment in which circularly polarized emission can potentially be produced through Faraday conversion (Ruszkowski & Begelman 2002).

Here we develop a numerical algorithm to carry out polarized radiative transfer through the TEMZ model. We have embedded this algorithm into the ray-tracing code RADMC3D (see <http://ascl.net/1202.015>), which we use to image the TEMZ grid. This makes it possible to compute both LP and CP intensity images as a function of both time and frequency that include the effects of Faraday rotation as well as LP to CP conversion. We combine the turbulently disordered magnetic field with an ordered component, varying the ratio between the two. The results can be compared to VLBI images as well as to single-telescope polarization measurements.

This paper is organized as follows: In §2 we summarize the TEMZ model, in §3 we outline the radiative transfer theory adopted in our study, and in §4 we list the model parameters and present an initial ray-tracing calculation through an ordered magnetic field. In §5 we investigate the effect turbulence has on the birefringence of the plasma, while in §6 we carry out a ray-tracing calculation through a disordered magnetic field. In §7 we compute integrated levels of fractional circular polarization, while in §8 we present synthetic multi-epoch observations. In §9 we explore internal Faraday rotation within the TEMZ model. In §10 we investigate how CP depends on plasma composition. In §11 we study spectral polarimetry. Finally, §12 contains our summary and conclusions.

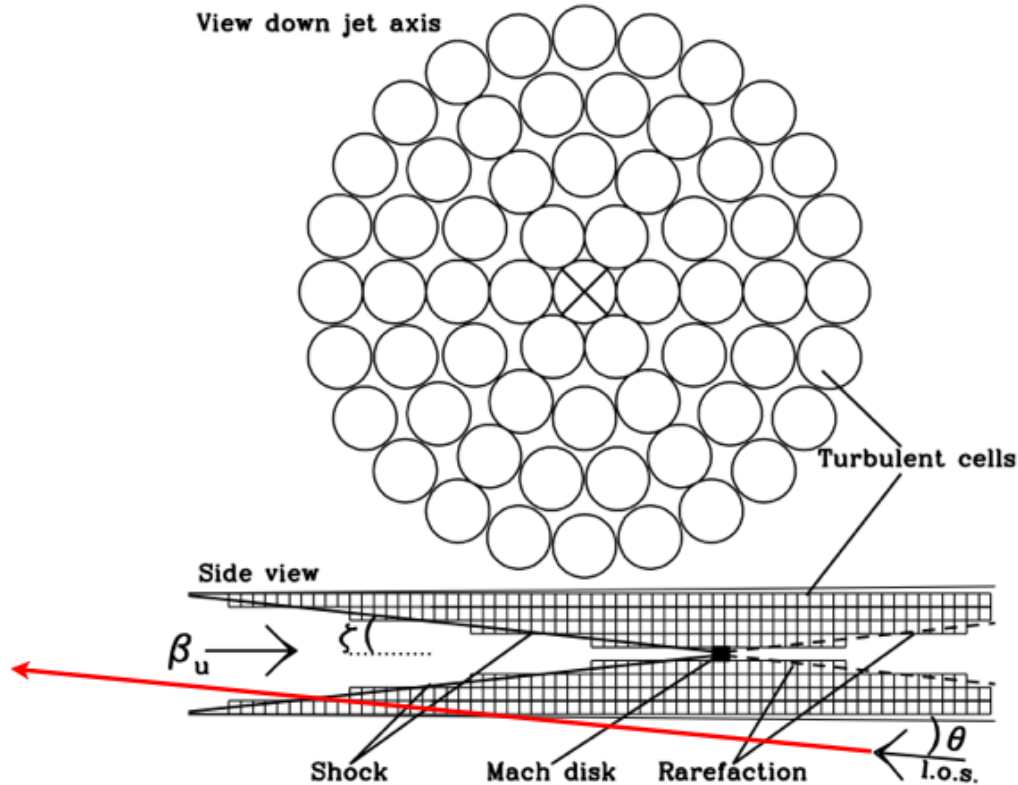


FIG. 1.— A schematic representation of the TEMZ model, reproduced from Marscher (2014) and MacDonald (2016). The radio core of a blazar is modeled as a collection of thousands of turbulent cells of plasma moving relativistically across a standing shock. The calculations presented in this study include 169 cells in the cross-section that includes the Mach disk (a small, transversely oriented shock, which is an optional feature), and a total of $\sim 13,000$ cells. The red line depicts how, along a given sight-line through the TEMZ grid, an individual ray crosses multiple cells of plasma, each with a distinct magnetic field orientation.

2. SUMMARY OF THE TEMZ MODEL

In the TEMZ code (Marscher 2014), the jet plasma is divided into thousands of cylindrical cells (as depicted in Figure 1), each with uniform physical properties. Simulated turbulence is realized through an adaptation of a scheme by Jones (1988), in which each cell belongs to four nested zones (with dimensions of $1 \times 1 \times 1$, $2 \times 2 \times 2$, $4 \times 4 \times 4$, and $8 \times 8 \times 8$ cells), with each zone contributing a fraction of the turbulent magnetic field and density of the cells that it contains. These contributions follow a Kolmogorov spectrum to determine the relation between the size of the zone and the fraction of the turbulent field component or electron density (which can include positrons as well) that the zone provides to its cells. An ordered component of the magnetic field can optionally be included, superposed on the turbulent field. The energy density of the particles injected at the upstream end of the jet varies according to a power-law red-noise spectrum. The magnitudes of the turbulent field and density of each zone are computed randomly within a log-normal distribution, while the direction of the field is also determined randomly at the upstream and downstream borders of the zone and rotated smoothly in between. This scheme qualitatively reproduces both the randomness of turbulence and correlations among turbulent cells located near each other. The direction of the turbulent velocity of each cell is chosen randomly (with magnitude set at a specified fraction of the sound speed), and this velocity is added vectorially to the systemic velocity.

The turbulence is assumed to endow the plasma with

relativistic electrons that follow a power-law energy distribution. When a plasma cell crosses a standing oblique (conical in three dimensions) shock in the millimeter-wave core, its electrons are heated solely via compression if the magnetic field is not close to parallel to the shock normal, or accelerated to considerably higher energies (while maintaining the power-law form) if the field is more favorably oriented (see, e.g., Sumerlin & Baring 2012). The component of the magnetic field lying perpendicular to the shock normal, as well as the density, are amplified by the shock compression. Downstream of the shock, a conical rarefaction decompresses the plasma; beyond this point the emission is considered to contribute only a small fraction of the flux and hence is ignored.

TEMZ computes the synchrotron emission and absorption coefficients in each cell as viewed by the observer, taking into account Doppler beaming, the aberrated direction of the magnetic field (see, e.g., Lyutikov, Pariev, & Gabuzda 2005), and light-travel delays. It also calculates inverse Compton emission and full time-dependent spectral energy distributions, but the present work is not concerned with these features.

3. POLARIZED RADIATIVE TRANSFER

In order to compute both LP and CP at radio frequencies, we need a numerical algorithm to solve the full Stokes equations of polarized radiative transfer (summarized in Jones & O’Dell 1977; Jones 1988). In particular, we solve the following matrix along individual rays passing through the TEMZ grid:

$$\begin{pmatrix} \left(\frac{d}{dl} + \kappa_I\right) & \kappa_Q & \kappa_U & \kappa_V \\ \kappa_Q & \left(\frac{d}{dl} + \kappa_I\right) & \kappa_V^* & -\kappa_U^* \\ \kappa_U & -\kappa_V^* & \left(\frac{d}{dl} + \kappa_I\right) & \kappa_Q^* \\ \kappa_V & \kappa_U^* & -\kappa_Q^* & \left(\frac{d}{dl} + \kappa_I\right) \end{pmatrix} \begin{pmatrix} I_\nu \\ Q_\nu \\ U_\nu \\ V_\nu \end{pmatrix} = \begin{pmatrix} \eta_\nu^I \\ \eta_\nu^Q \\ \eta_\nu^U \\ \eta_\nu^V \end{pmatrix} \quad (1)$$

Here, I_ν , Q_ν , U_ν , and V_ν are the frequency-dependent Stokes parameters, while $(\eta_\nu^I, \eta_\nu^Q, \eta_\nu^U, \eta_\nu^V)$ and $(\kappa_I, \kappa_Q, \kappa_U, \kappa_V)$ represent, respectively, the emission and absorption coefficients for the corresponding Stokes parameters. The effects of Faraday rotation and conversion are governed by the κ_V^* and (κ_Q^*, κ_U^*) terms, respectively. Finally, the path length through each cell of plasma is given by l . This matrix has an analytic solution outlined in Jones & O'Dell (1977). We apply this analytic solution along individual rays passing through the TEMZ grid (depicted by a red line in Figure 1), following the polarized radiative transfer from cell to cell.

We embed this polarized radiative transfer scheme into the ray-tracing code RADMC3D. This code allows one to cast thousands of rays through the TEMZ grid, producing synthetic maps of the resultant polarized emission. The exact analytic solutions to Equation 1 for I_ν , Q_ν , U_ν , and V_ν , as well as an expression for the optical depth τ of each TEMZ cell, are given in Appendix A. RADMC3D was designed to handle radiative transfer through non-relativistic media. Analytic expressions that account for the effects of relativistic aberration of the rays cast by RADMC3D are also outlined in Appendix A. In §5 and Appendix A we carry out several tests of our algorithm.

4. RAY-TRACING THROUGH AN ORDERED MAGNETIC FIELD

Table 1 lists the various adjustable parameters of the TEMZ code, which include the ratio of ordered magnetic field to the mean turbulent field, the parameter of greatest importance to the present study. As an initial test of the polarized radiative transfer algorithm, we have performed a ray-tracing calculation through the vector-ordered magnetic field shown in Figure 2. For this calculation (and the computations below), the TEMZ grid is composed of over 13,000 individual plasma cells grouped into eight concentric cylindrical shells forming the recollimation shock depicted in Figure 1. These cells of plasma were then mapped onto a uniform $120 \times 120 \times 120$ cartesian grid through which the ray-tracing calculation was performed. This grid was input into the RADMC3D code, which cast 640,000 individual rays forming 800×800 square-pixel maps of the resultant polarized emission. RADMC3D uses a first-order cell-based scheme in which the path length (l) through each cell is determined and all plasma quantities are zone-centered. The image maps from this first ray-tracing are shown in Figure 3.

TABLE 1
TEMZ MODEL PARAMETERS AND VALUES USED IN THIS STUDY

Symbol	Description	Value
Z	Redshift	0.069
α	Optically thin Spectral index	0.65
B	Mean magnetic field (G)	0.1
$-b$	Power-law slope of power spectrum	1.7
f_B	Ratio of energy densities u_e/u_B	0.03
R_{cell}	Radius of TEMZ cells (pc)	0.004
γ_{max}	Maximum electron energy	10000
γ_{min}	Minimum electron energy	1000
β_{u}	Bulk laminar velocity of unshocked plasma	0.986
β_{t}	Turbulent velocity of unshocked plasma	0.0
ζ	Angle between conical shock and jet axis	10°
θ_{obs}	Angle between jet axis and line of sight	6°
ϕ	Opening semi-angle of jet	1.9°
z_{MD}	Distance of Mach disk from BH (pc)	1.0
f_{field}	Ratio of ordered helical field to total field	0.1-1.0
ψ	Pitch angle of the helical field	85°
n_{step}	Number of time steps	5000
n_{rad}	Number of cells in jet cross-section	169

The angle of inclination of the jet to the line of sight was set to 6° , and the jet was given a bulk Lorentz factor of $\Gamma = 6$. Each plasma cell was assigned a characteristic length scale of 0.004 pc. An underlying electron power-law energy distribution, $n_e(\gamma) \propto \gamma^{-s}$, was assumed to hold over an energy range γ_{min} to γ_{max} , with $s = 2.3$ applied throughout the grid. After a cell crosses the shock, the values of γ_{min} and γ_{max} are computed as the electrons suffer radiative cooling. Table 1 lists the values of the other TEMZ model parameters used in our calculations. Figure 3 shows maps of the fractional circular polarization ($m_c = -V/I$) emerging from the TEMZ grid. Unlike observations that typically show only one sign of CP in a given blazar, these synthetic maps contain both positive and negative CP that appear simultaneously. The levels of circular polarization in these maps reach $\sim 3\%$. The highest levels of circular polarization observed to emanate from an extragalactic jet are $\sim 2 - 4\%$ in the radio galaxy 3C 84 (Homan & Wardle 2004). These preliminary results are encouraging, but the magnetic field structure used here is highly idealized and is unlikely to be realized in the astrophysical context of an actual blazar jet.

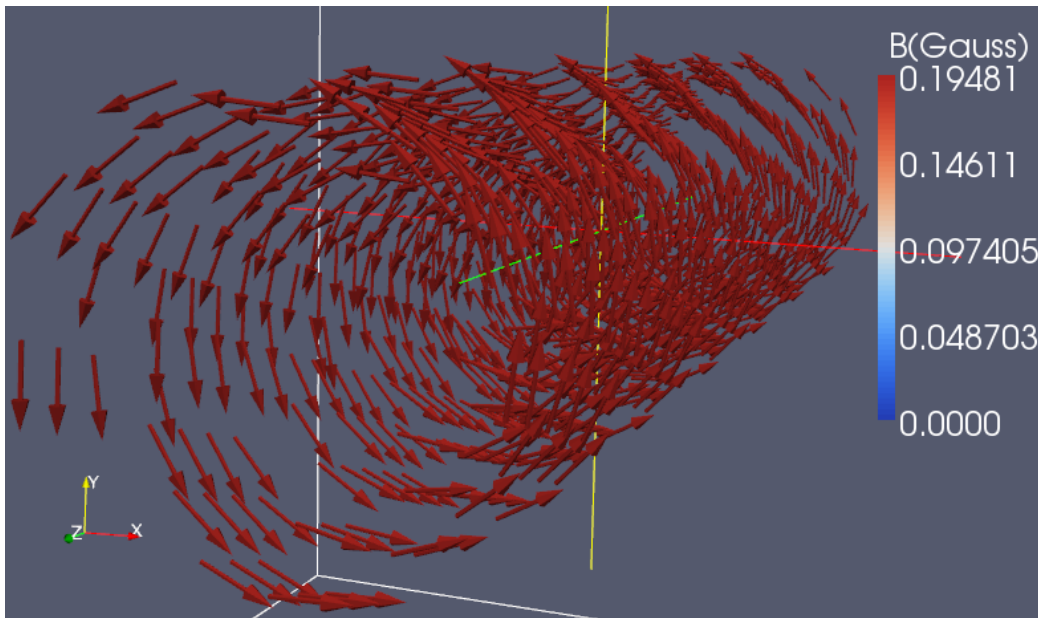


FIG. 2.— A rendering of the three-dimensional distribution of well-ordered magnetic field within the TEMZ grid. Each vector depicts the magnetic field orientation within an individual plasma cell and is color-coded according to the strength of the field (see color bar to the right).

5. FARADAY CONVERSION IN A DISORDERED MAGNETIC FIELD

After performing the initial ray-tracing calculation presented in §4, we applied our scheme to the case of a turbulent magnetic field. One would expect that the increased disorder in the field would increase the birefringence of the jet plasma, leading to increased Faraday conversion, as found by Ruszkowski & Begelman (2002). It might also cause depolarization of the emission due to the lack of a systematic vector-ordered magnetic field component. The interplay between these two effects should govern the level of CP produced in a turbulent TEMZ grid. In order to explore these effects in a quantifiable manner, we have tracked several emission parameters pertaining to CP production along a random sight-line through the TEMZ model. As a first test, we recorded the fractional CP (m_c) from cell to cell along a given sight-line (see upper panel of Figure 4). In one test case (shown in red in the upper panel of Figure 4), we plot only the fractional CP intrinsic to each cell. In another test case (shown in blue in the upper panel of Figure 4), we also allow Faraday conversion to attenuate the emission from cell to cell along our sight-line. One can clearly see that as our ray passes through the turbulent plasma, Faraday conversion increases the observed level of m_c beyond what would be intrinsic to each cell. We also call attention to the high levels of m_c that are produced within the TEMZ model ($\sim 15\%$ for this particular sight-line). These “extreme” CP pixels get “washed” out when we convolve our resolved emission maps with a circular Gaussian beam (illustrated in §6.7 below), resulting in integrated levels of CP $m_c \sim 2\text{--}3\%$.

As summarized in Wardle & Homan (2003) and Ruszkowski & Begelman (2002), the production of CP within blazars most likely results primarily from Faraday conversion in a turbulent jet plasma. This process occurs over two stages. Initially, linearly polarized emission originates from within the jet via synchrotron emis-

sion from relativistic electrons entrained in the jet’s magnetic fields. If we choose a suitable reference axis, this process will generate Stokes Q. Internal Faraday rotation then converts Q into U as the synchrotron radiation propagates through regions with different field orientations (the cells in the TEMZ model), which act as internal Faraday screens (see §9). Faraday conversion, a process uniquely intrinsic to relativistic plasma, then transforms U into V. Therefore, the production of CP within a blazar jet is dependent upon both the Faraday rotation depth (τ_F) and the Faraday conversion depth (τ_C) through the intervening jet plasma along the line of sight. These Faraday depths are themselves dependent upon the optical depth (τ) of the jet plasma:

$$\tau_F = \zeta_V^* \tau \quad (2)$$

and

$$\tau_C = \zeta_Q^* \tau, \quad (3)$$

where ζ_V^* , ζ_Q^* , and τ are given in Appendix A; their values are specific to the synchrotron process (see Equations A2, A11, and A12, respectively). It then follows that the observed levels of fractional CP are proportional to these Faraday depths, $m_c \propto \tau_F \tau_C$. As a second test of CP production in the TEMZ grid, in the lower panel of Figure 4 we plot the Faraday rotation and conversion depths from cell to cell along the same sight-line shown in the upper panel of Figure 4. While the conversion depth τ_C of each cell remains fairly small along this particular sight-line, we do indeed see a marked increase (in degree) of the rotation depth τ_F along the ray. It is plausible that this increased internal Faraday rotation towards the edge of the jet drives the increase in CP present in the upper panel of Figure 4. An additional test of our CP algorithm is presented in the final section of Appendix A.

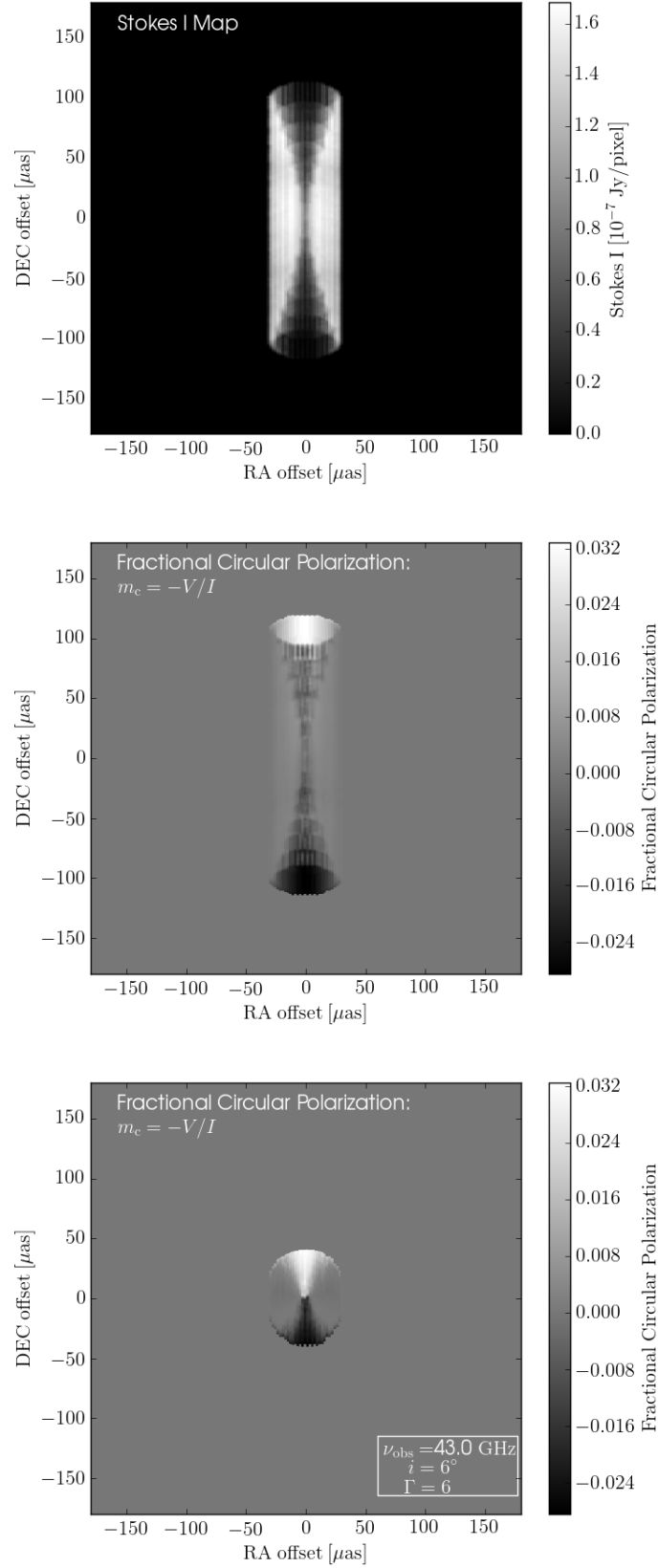


FIG. 3.— **(Upper panel)** - A rendering of the total intensity I in the co-moving frame highlighting the structure of the TEMZ computational grid. The magnetic field has the ordered structure displayed in Figure 2. **(Middle panel)** - A plot of the fractional CP in the co-moving frame highlighting the different regions within the jet that produce positive and negative CP. **(Lower panel)** - A plot of the fractional CP in the observer's frame at an observing frequency of 43 GHz.

6. RAY-TRACING THROUGH A DISORDERED MAGNETIC FIELD

We proceed to explore the effect that a more turbulent jet environment would have on the CP emission maps produced by RADMC3D. Figure 5 illustrates the more disordered magnetic field used in our second calculation. All of the model parameters listed in Table 1 remain the same as for the ordered field computations, except here f_{field} , the ratio of the ordered helical magnetic field to the total magnetic field within each TEMZ cell, is set to 0.1 (Figure 5). As discussed in §5, the expectation is that the increased disorder in the turbulent TEMZ field will lead to increased levels of CP. The images from this second ray-trace are shown in Figures 6 and 7. We convolve these resultant images with a circular Gaussian beam with a full width at half maximum (FWHM) of $\sim 14 \mu\text{as}$ that is small enough to illustrate the main features of the images. The increased level of turbulence in this simulation is evident in every image. We also convolve the images (shown in Appendix B) with a beam of FWHM $\sim 50 \mu\text{as}$ that roughly corresponds to the angular resolution of the longest baselines of a global VLBI array (or one including an antenna in space) at short radio wavelengths, for comparison with potential future observations.

The integrated levels of circular polarization ($\overline{m_c}$, shown in the middle panel of Figure 7, and discussed in detail in §7 below) reach $\sim 2.6\%$, which is still in rough agreement with observations of circular polarization in blazars (see Homan & Wardle 2004). However, we find very localized levels of fractional circular polarization that can reach as high as $\sim 15\%$ in a disordered (upstream of the shock) TEMZ field (see upper panel of Figure 4 and Figure 14 in Appendix A). In all instances the fractional LP (m_l) is much larger than the fractional CP (m_c); however, m_l always remains below 71% (the theoretical maximum for synchrotron emission with $\alpha = 0.65$; Pacholczyk 1970). The dashed white line in the upper left panel of Figure 6 delineates an area within which we compute several additional emission properties (see §7). The images presented in Figure 6 are obtained at an observing frequency of $\nu_{\text{obs}} = 43 \text{ GHz}$. The I map is positive definite. The Q, U, and V maps exhibit a range of positive and negative values. In Figure 6 we plot only positive values for ease of visualization. A study of the temporal and spectral variability of these synthetic image maps is presented in §8 and §11. An animation of the temporal variability in each of the Stokes parameter maps over the course of the 5000 time steps of the simulation (roughly 1000 days in the observer's frame) can be viewed at <http://people.bu.edu/nmacdona/Research.html>.

The upper panel of Figure 7 presents a map of linearly polarized intensity ($P \equiv \sqrt{Q^2 + U^2}$). The orientation of the LP as projected onto the plane of sky is demarcated by electric vector position angles (EVPAs) χ . These EVPAs are shown as black line segments in the upper panel of Figure 7. The value of χ within a given pixel is computed based on the local values of Q and U within that pixel: $\chi = \frac{1}{2} \arctan(U/Q)$. As a further test of our algorithm, we tune our observing frequency until the emission emanating from the TEMZ grid reaches the optically thick limit. As $\tau \rightarrow 1$ we observe the polarization vectors to rotate by 90° , as predicted by the theory

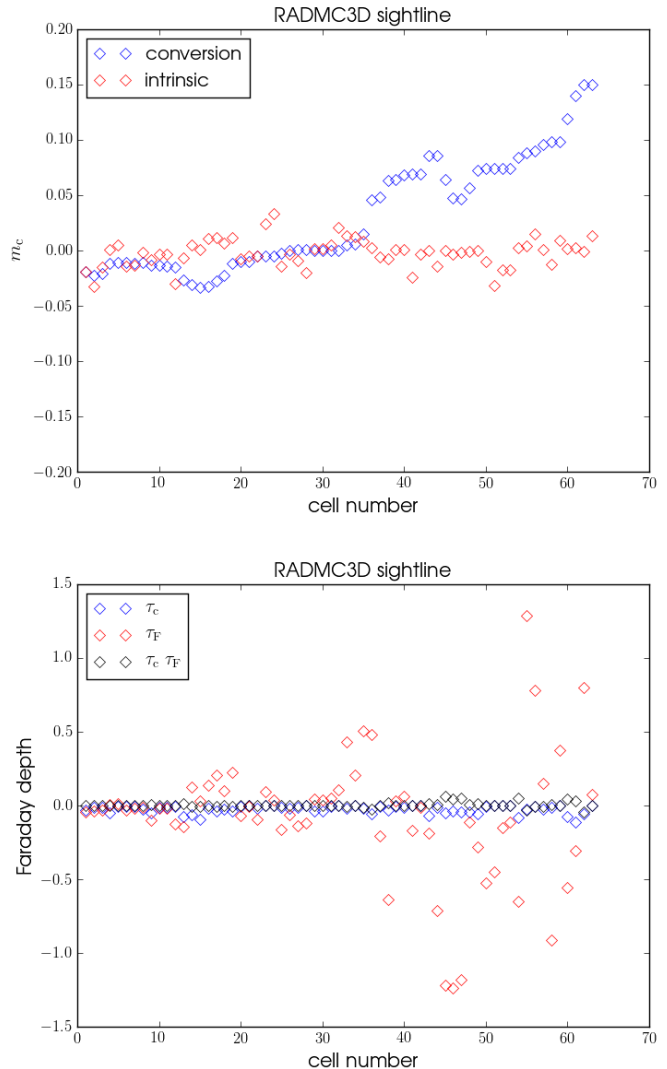


FIG. 4.— **(Upper panel)** - A plot of fractional circular polarization m_c along a random sight-line through the TEMZ grid. The red diamonds correspond to CP intrinsic to each TEMZ cell, whereas the blue diamonds highlight the effect that Faraday conversion has on the observed level of CP along the ray. The radiative transfer starts at the back of the jet (cell 0) and progresses to the front of the jet (cell 70), resulting in the creation of one pixel in our image maps. **(Lower panel)** - A plot of Faraday rotation depth τ_F (red diamonds), Faraday conversion depth τ_C (blue diamonds), and their product $\tau_C \tau_F$ (black diamonds), along the same sight-line presented in the upper panel. The cell numbers are identical.

of synchrotron self-absorption (Pacholczyk 1970). Images obtained of the polarized intensity in the co-moving frame of the plasma (similar to Figure 3) clearly show ordering of the initially turbulent magnetic field downstream of the shock.

For all of the calculations presented in this paper, the angle of the jet to our line of sight (θ_{obs}) is set to 6° . All of our model parameters are similar to those used by Wehrle et al. (2016) to model BL Lacertae. In the future, we plan to carry out a more detailed study of the effect that varying degrees of jet inclination can have on the observed levels of CP. This test will be crucial in determining whether the sign of m_c is sensitive to the large scale orientation of the jet's magnetic field with

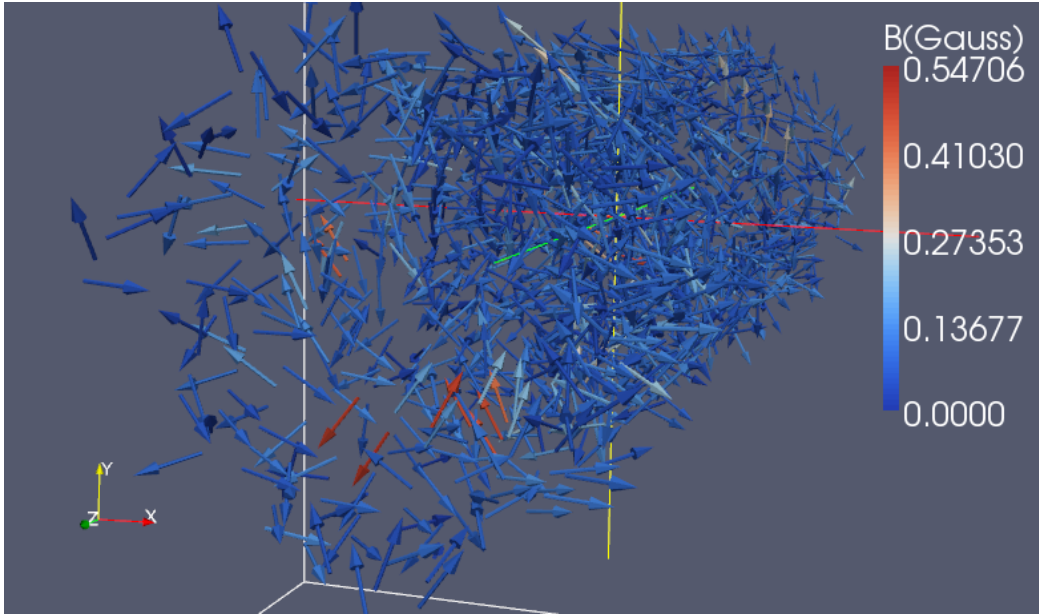


FIG. 5.— A rendering of the three-dimensional distribution of an initially disordered magnetic field, after partial ordering by a conical standing shock, within a turbulent TEMZ grid. As in Figure 2, each vector depicts the magnetic field orientation within an individual plasma cell, and is color-coded according to the strength of the field (see color bar to the right).

respect to our line of sight (see Enßlin 2003; Ruszkowski & Begelman 2002).

7. INTEGRATED LEVELS OF FRACTIONAL POLARIZATION

At the resolution of VLBI polarized intensity images published thus far, the structure displayed in Figures 6 and 7 would only be partially resolved or even unresolved. In order to make comparisons between the levels of CP present in our simulations and existing measurements, we therefore compute integrated levels of fractional CP and LP. This is accomplished by first defining an annulus around the jet emission in our initial I map (the white dashed circle in the upper left panel of Figure 6). We then compute $m_c = -V/I$ and $m_l = \sqrt{Q^2 + U^2}/I$ in each pixel within this annulus, creating the maps of fractional polarization shown in Figure 7. To acquire integrated levels of polarization, we then compute averages of the four Stokes parameters within the annulus: \bar{I} , \bar{Q} , \bar{U} , and \bar{V} . Based on these averages, we compute integrated levels of fractional circular polarization:

$$\bar{m}_c = -\bar{V}/\bar{I}, \quad (4)$$

and fractional linear polarization (see Figure 7):

$$\bar{m}_l = \sqrt{\bar{Q}^2 + \bar{U}^2}/\bar{I}. \quad (5)$$

As discussed in §6, the levels of fractional polarization present in Figure 7 are in rough agreement with observations of CP. In §8 below, we carry out a temporal analysis in which we monitor these integrated levels of polarization over the course of the entire TEMZ simulation. The presence of both negative and positive levels of CP (simultaneously) within our maps is a distinct feature that has not been seen in observations of blazar jets, but this may be the result of the cores only being partially resolved by VLBI observations. It will be of interest to compare our LP synthetic images with the results of upcoming observational campaigns that will image several

blazars on $\sim 50 \mu\text{as}$ scales with various VLBI arrays, including RadioAstron plus ground based antennas, the Global Millimeter VLBI Array (GMVA), and the Event Horizon Telescope (EHT). The sensitivity and resolution of these combined arrays should be sufficient to probe the location(s) in the jet where Faraday conversion occurs.

8. MULTI-EPOCH OBSERVATIONS

There have been several multi-frequency studies of the temporal variability of CP observed in blazar jets. In particular, the University of Michigan Radio Astronomy Observatory (UMRAO) has carried out several dedicated programs with single 26 m dish observations at frequencies of 4.8, 8.0, and 14.5 GHz (see, e.g., Aller, Aller, & Hughes 2011; Aller, Aller, & Plotkin 2003). These campaigns have detected CP at faint but statistically significant levels in a number of blazar jets (e.g., 3C 273, 3C 279, 3C 84, and 3C 345). A marked feature in the temporal variability of CP in these sources is the occurrence of sign reversals in the handedness of the observed fractional CP. These sign changes occur over a range of timescales (month to years). It has been suggested that these sudden reversals in the sign of m_c indicate the existence of turbulent magnetic fields within the radio cores of these objects (see Aller, Aller, & Plotkin 2003). Enßlin (2003) pointed out, however, that there are long time spans (decades in some cases) over which the sign of m_c can remain constant. Enßlin suggested that in these objects Faraday conversion occurs as the radio waves propagate through a rotationally twisted rather than turbulent magnetic field. Since the twist could result from rotation of the field lines at the base of the jet (e.g., if the footprint of the field is in plasma orbiting the black hole), CP sign reversals would be quite rare. These two physical scenarios highlight the potential of using observations of temporal variability in CP as a probe of the underlying physics of jets.

In order to investigate these two scenarios, we have carried out a time series analysis of the integrated lev-

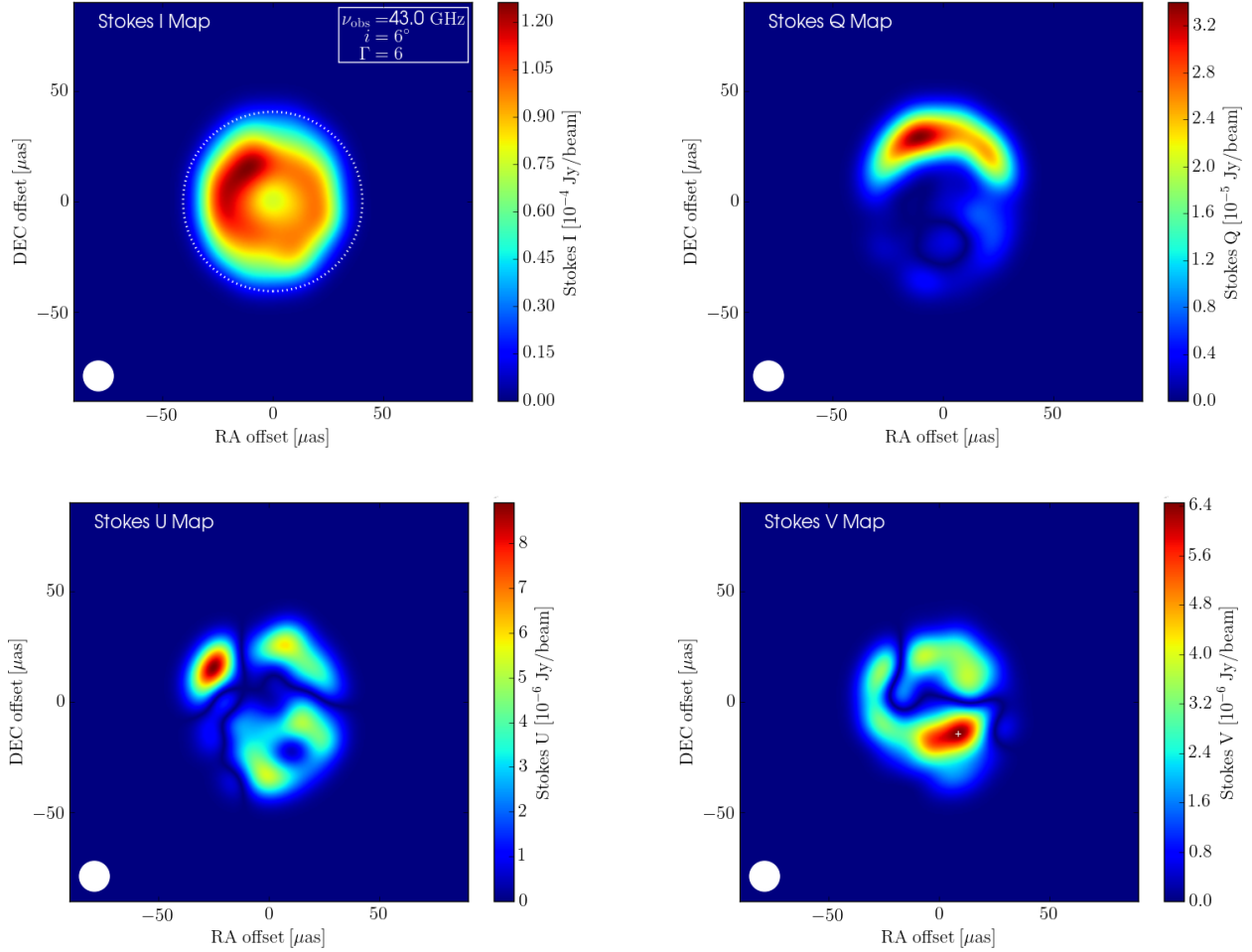


FIG. 6.— **(Upper left panel)** - Total intensity (I) map at an observing frequency of 43 GHz. The white dashed circle defines an arbitrary region within which we compute fractional CP (m_c) and LP (m_l) (presented in Figure 7). **(Upper right panel)** - Q map. **(Lower left panel)** - U map. **(Lower right panel)** - V map. We compute the mean optical ($\bar{\tau} \sim 0.009$ - Equation A2), Faraday rotation ($\bar{\tau}_F \sim 0.09$ - Equation 2), and Faraday conversion ($\bar{\tau}_C \sim 0.01$ - Equation 3) depths along the sight-line demarcated by a white cross on this map. At $\nu_{\text{obs}} = 43$ GHz the emission produced by the TEMZ model is in the optically thin regime. Plots of the cell-to-cell variations of these quantities along this particular sight-line (and at frequencies of $\nu_{\text{obs}} = 15$ and 22 GHz) are shown in Figure 17 in Appendix B. The above images have all been convolved with the circular Gaussian beam shown in the lower left of the respective panels.

els of fractional CP produced by the TEMZ model using two different magnetic field grids: (i) the ordered helical magnetic field geometry presented in Figure 2, and (ii) the turbulent magnetic field depicted in Figure 5. We have run the TEMZ model over 5000 time steps. Each time step (as outlined in Marscher 2014) is determined by how long it takes one plasma cell to advect down the jet by one cell length (see Figure 1). With a bulk Lorentz factor $\Gamma = 6$ and viewing angle of 6° (Table 1), this corresponds to ~ 0.207 days in the observer's frame. All images in our time series analysis have been convolved with a circular Gaussian beam, one much smaller than that of current VLBI arrays, and one comparable to the highest resolutions available at present. Finally, as illustrated in Figures 6 and 7, we compute integrated levels of fractional circular polarization \bar{m}_c based on averages of V and I computed within an annulus surrounding the jet emission. These integrated values are then recorded from one time step to the next, creating synthetic multi-epoch observations. We perform this analysis for both grids at frequencies of $\nu_{\text{obs}} = 15, 22$, and 43 GHz. The

results are shown in Figure 8, in which the upper panel illustrates the temporal variability in \bar{m}_c for the ordered field case, whereas the lower panel highlights the corresponding variability in \bar{m}_c for a disordered field. The average value of \bar{m}_c for each TEMZ run is listed (for each frequency) in the lower right of each panel. The sign of m_c over multiple epochs in the ordered field case, is in keeping with the predictions of Ruszkowski & Begelman (2002) and Enßlin (2003). In contrast, when the field is disordered, we indeed see successive reversals in the sign of \bar{m}_c . At $\nu_{\text{obs}} = 43$ GHz the value of \bar{m}_c is predominantly positive for both runs, whereas at $\nu_{\text{obs}} = 15$ and 22 GHz the value of \bar{m}_c tends to be negative. In §11 below we carry out a more detailed analysis of the spectral behavior of $m_c(\nu)$. The temporal variability of m_c for a disordered field supports the interpretation proposed by Aller, Aller, & Hughes (2011) that reversals in the sign of CP are an observational signature of turbulence within the jet plasma. We also find a sizable difference in the overall level of CP between the ordered and disordered magnetic field models, as discussed in §5.

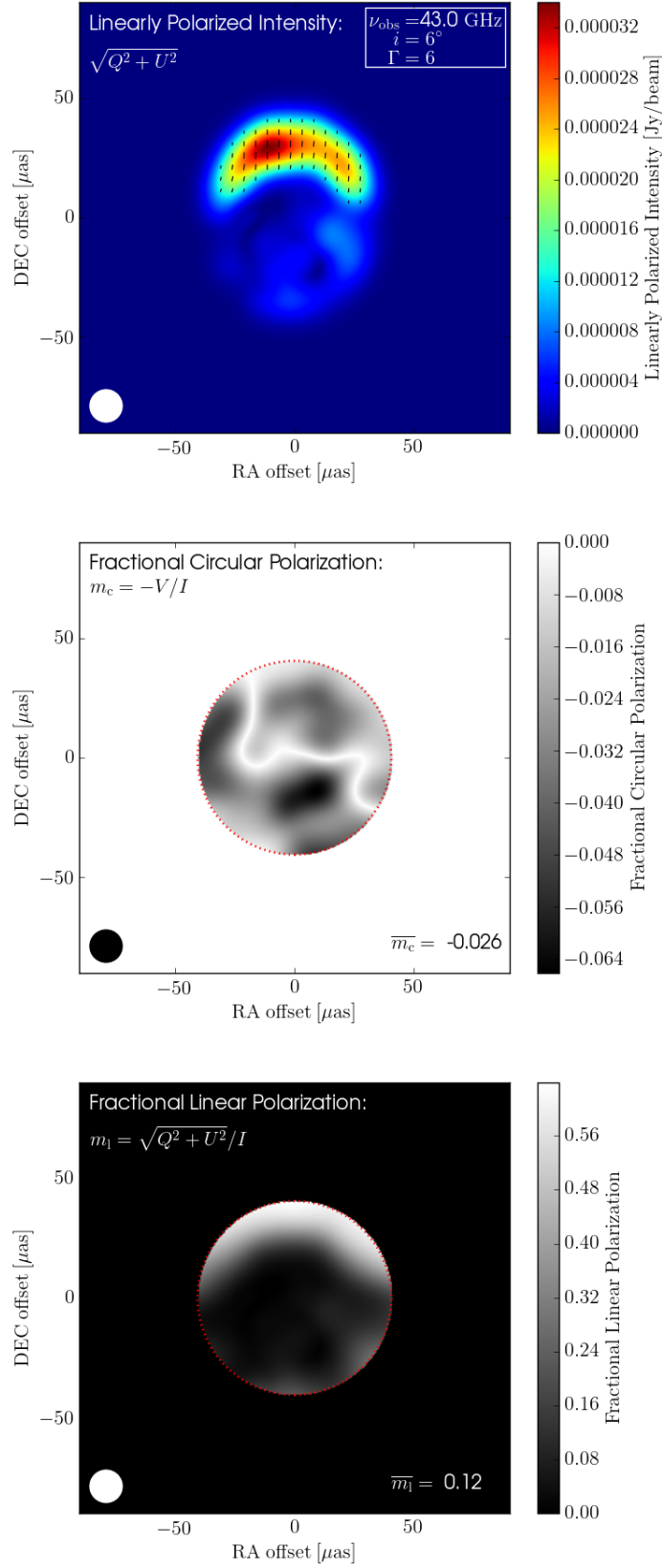


FIG. 7.— **(Upper panel)** - Rendering of linearly polarized intensity P of the disordered TEMZ grid at an observing frequency of 43 GHz. Black line segments indicate the electric vector position angles (EVPAs) as projected onto the plane of the sky. The effects of relativistic aberration (see Lyutikov, Pariev, & Gabuzda 2005) on the orientation of these EVPAs have been included in these calculations. **(Middle panel)** - Map of observed fractional CP, with an integrated value ($\overline{m_c}$) given in the lower right. **(Lower panel)** - Map of observed fractional LP, with an integrated value ($\overline{m_l}$) given in the lower right. The above images have all been convolved with the circular Gaussian beam shown in the lower left of the respective panels.

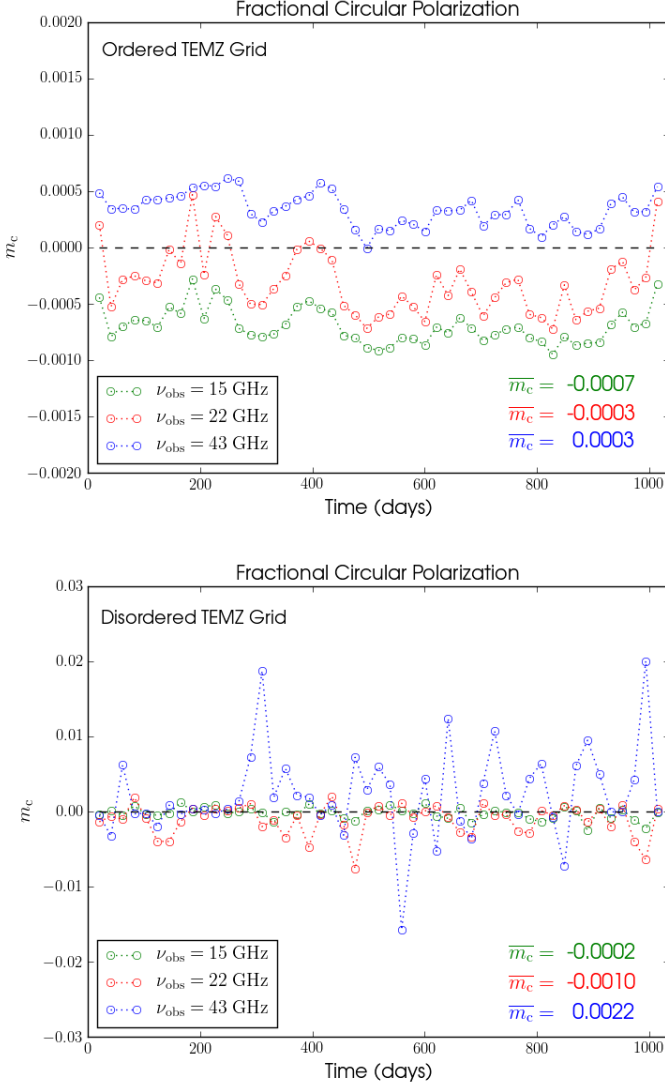


FIG. 8.— **(Upper panel)** - Variations of m_c for the ordered field case (see Figure 2). The simulation is run for 5000 time steps, with each time step corresponding to 0.207 days in the observer’s frame. The green, red, and blue points correspond to observations at $\nu_{\text{obs}} = 15, 22$, and 43 GHz, respectively. The average values of m_c for each frequency over the duration of the simulation are listed in the lower right. **(Lower panel)** - Corresponding variability in m_c for the disordered field case (see Figure 5).

9. INTERNAL FARADAY ROTATION

After creating synthetic radio images of the TEMZ model at $\nu_{\text{obs}} = 43$ GHz (§6 & §7), we proceeded to map the amount of internal Faraday rotation occurring within the jet. In Figure 9, we present a map of the degree ($\Delta\chi$):

$$\Delta\chi = |\chi_{\zeta_V^*} - \chi_{\zeta_V^* \rightarrow 0}|, \quad (6)$$

by which the orientation of the observed LP angle (χ) is rotated by in each pixel between a ray-tracing calculation in which we include the effects of Faraday rotation within the plasma (ζ_V^* ; as discussed in §5, see Equation 2) and an identical calculation in which we suppress the effects of Faraday rotation within the plasma ($\zeta_V^* \rightarrow 0$). If the Faraday rotation is internal to the jet (as is the case here, since there is no plasma external to the jet in our

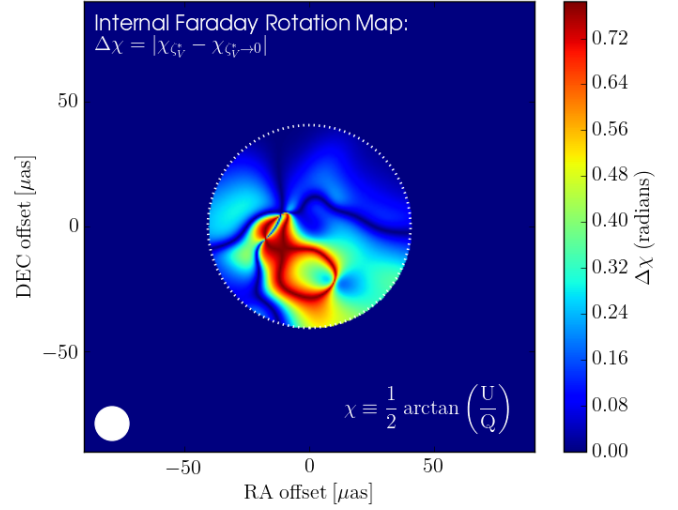


FIG. 9.— An internal Faraday rotation map of the TEMZ model at $\nu_{\text{obs}} = 43$ GHz. At each pixel within the white dashed annulus, we have computed the absolute difference in EVPA angle (χ) between a ray-tracing calculation in which we include the effect of Faraday rotation (ζ_V^*) and one in which we suppress Faraday rotation within the plasma ($\zeta_V^* \rightarrow 0$).

computations), this degree of rotation will be:

$$\Delta\chi \propto \tau_f \propto \frac{\ln \gamma_{\min}}{\gamma_{\min}^{2\alpha+2}} \Lambda \quad (7)$$

(Wardle & Homan 2003). In Equation 7, τ_f is the Faraday rotation depth through the jet plasma, γ_{\min} is the lower limit of the electron power-law energy distribution, and $\Lambda (\equiv f_l f_u)$ is equal to the product of the lepton charge number of the plasma (f_l) with the fraction of magnetic field that is in an ordered component (f_u). Here,

$$f_l = \frac{(n_- - n_+)}{(n_- + n_+)}, \quad (8)$$

where $n_-/+$ are the number densities of the electrons/positrons respectively. Within each TEMZ cell the magnetic field is vector-ordered and unidirectional, implying $f_u \rightarrow 1$. We explore different plasma compositions in §10, but for this calculation we assume a normal plasma with no positrons ($n_+ = 0$ & $f_l \rightarrow 1$). As with our maps of fractional linear and circular polarization (Figure 7), we only compute $\Delta\chi$ within the white dashed annulus shown in the upper left panel of Figure 6. We find very localized regions of relatively high rotation ($\Delta\chi \sim 0.7$ rad at 43 GHz). It is within these regions that Faraday conversion (which is also proportional to τ_f) should drive the production of CP. It is useful to compare our map of Stokes V (lower right panel of Figure 6) to the above map of Faraday rotation. The rough similarity of these figures highlights the potential of using polarimetric observations obtained on scales of tens of μas to constrain where in blazar jets CP is being produced through Faraday conversion.

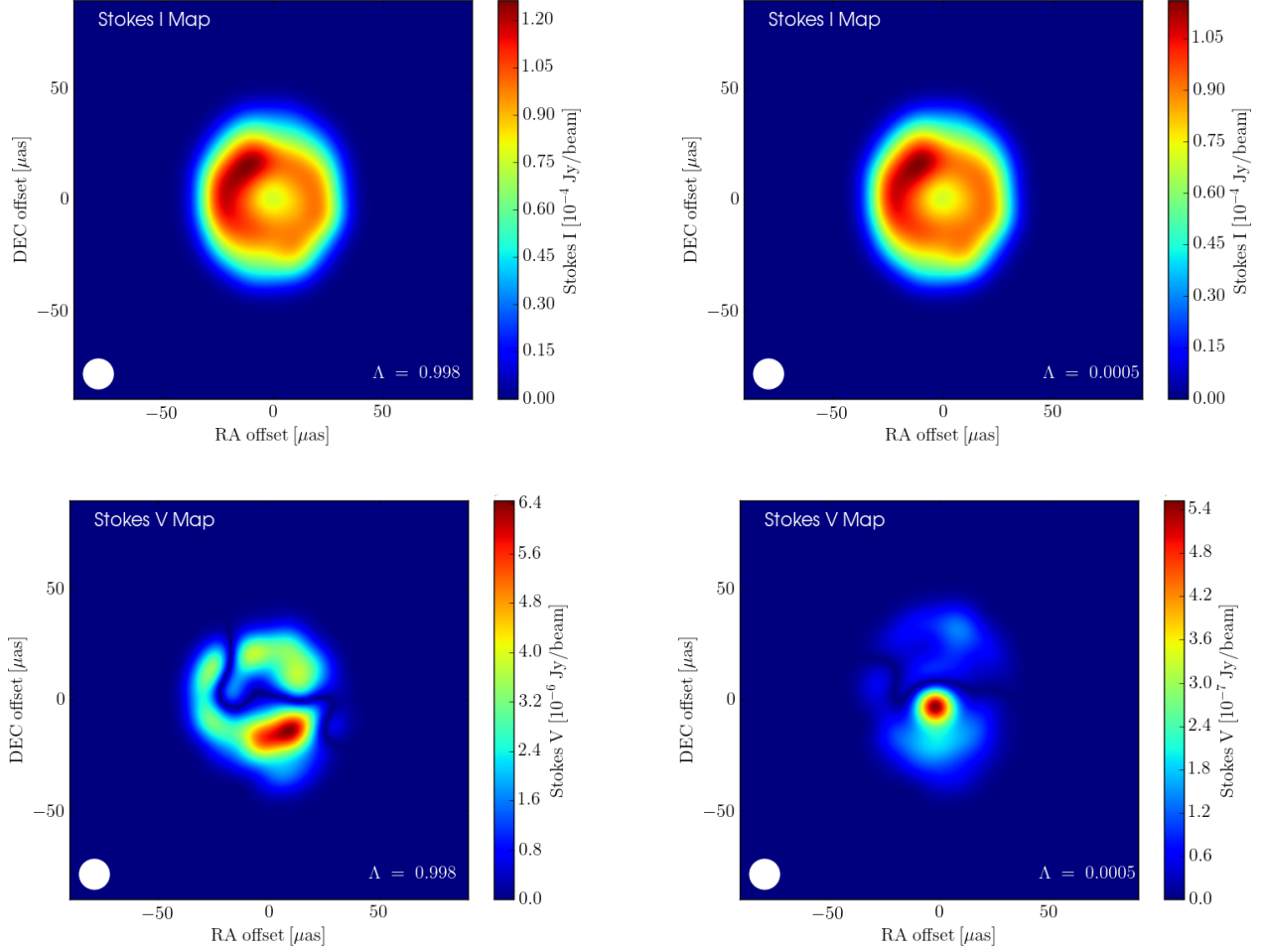


FIG. 10.— **(Upper left panel)** - I map for a jet composed mainly of “normal” plasma with a proton to positron ratio of 1000 ($\Lambda = 0.998$). **(Upper right panel)** - I map for a jet with plasma dominated by pairs (proton to positron ratio of 0.001; $\Lambda = 0.0005$). **(Lower left panel)** - Corresponding V map for the normal plasma case. **(Lower right panel)** - Corresponding V map for the pair plasma case. The above images have all been convolved with the circular Gaussian beam displayed in the lower left of the respective panels. All images are produced from the same TEMZ grid at $\nu_{\text{obs}} = 43$ GHz. The difference in the CP emission between the lower left and lower right panels highlights the sensitivity of CP to the underlying plasma content of the jet.

10. PLASMA COMPOSITION STUDY

The calculations presented above (§§4-9) have assumed a pure electron-proton plasma within the jet ($\Lambda = 1$). Some admixture of positrons within the jet plasma should also be explored. In order to incorporate plasma composition into our ray-tracing calculations, we have modified the following emissivity term in our polarized radiative transfer routine (see Appendix A, Equation A12, and Homan et al. (2009) for a more complete discussion) to include a term accounting for the plasma content of the jet:

$$\zeta_V^* = \zeta_\alpha^{*V} (\nu/\nu_{\min})^{\alpha+\frac{1}{2}} \frac{\ln \gamma_{\min}}{\gamma_{\min}} \cot(\vartheta) \Lambda \left[1 + \frac{1}{2\alpha+3} \right],$$

where $\Lambda = f_l f_u$. Within an individual TEMZ cell, the local magnetic field vector is uniform and unidirectional, implying $f_u = 1$, while f_l is given in §9 above (Equation 8). The number density of protons is $n_p = n_- - n_+$, since astrophysical plasmas are electrically neutral. In our computations, a “normal” plasma is assigned a proton to positron ratio of 1000 ($\Lambda = 0.998$),

while for a pair plasma the ratio is set at 0.001 ($\Lambda = 0.0005$). Figure 10 presents a comparison of the resultant emission from snapshots of the TEMZ results with the two different plasma compositions. It is evident in these images that CP is indeed a highly sensitive probe of the plasma content of the jet.

11. SPECTRAL POLARIMETRY

As discussed in §5, there are two distinct physical processes by which circularly polarized emission can be produced within a relativistic jet. CP can emanate either *intrinsically* (*int*) from synchrotron emission or through Faraday *conversion* (*con*); Jones & O’Dell (1977). The latter process is commonly believed to be the dominant form of CP production within blazars (Wardle et al. 1998; Ruszkowski & Begelman 2002). The spectral behavior of CP can be used to discern which of these two mechanisms of CP production dominates within the jet plasma, since:

$$m_C^{\text{int}} \propto \nu^{-1/2}, \quad (9)$$

whereas

$$m_C^{\text{con}} \propto \nu^{-3}. \quad (10)$$

O’Sullivan et al. (2013) have measured, with unprecedented sensitivity, both the degree and spectral behavior of CP, $m_C(\nu)$, in the quasar PKS B2126–158 using the Australia Telescope Compact Array (ATCA). They find that the fractional LP: $m_l(\nu)$, and the fractional CP: $m_c(\nu)$, are anti-correlated across a frequency range of $\nu_{\text{obs}} = 1\text{--}10$ GHz. This spectral behavior favors the conversion (*con*) mechanism of CP production. We have created synthetic spectral polarimetric observations of the TEMZ model over a range of frequencies (shown in Figure 11). We find that our plot of $m_c(\nu)$ lies between the two predicted curves for the intrinsic and conversion mechanisms. This would seem to indicate that both physical mechanisms contribute to the observed levels of CP within the TEMZ model (as is evident in the upper panel of Figure 4). We find that both $m_l(\nu)$ and $m_c(\nu)$ increase between $\nu_{\text{obs}} = 20$ and 60 GHz. In the 60–140 GHz range, $m_l(\nu)$ continues to increase and $m_c(\nu)$ decreases. It should be emphasized, on the other hand, that our synthetic observations are on vastly different scales compared to those presented in O’Sullivan et al. (2013).

12. SUMMARY AND CONCLUSIONS

We have found that a turbulent magnetic field partially ordered by a shock can produce circularly polarized emission at the percent levels seen in some blazars. We have demonstrated that Faraday conversion is indeed the dominant mechanism of CP production within the TEMZ model, in agreement with Jones (1988) and Ruszkowski & Begelman (2002). We have also shown that reversals in the sign of the integrated levels of m_C are indicative of turbulent magnetic fields within the jet (as postulated by Aller, Aller, & Plotkin 2003), while constancy in the sign of m_C over many epochs can indeed be attributed to the presence of large scale ordered helical magnetic fields within the jet (as predicted by Enßlin 2003).

We have created a map of the internal Faraday rotation present within the TEMZ model at $\nu_{\text{obs}} = 43$ GHz (Figure 9). The rough similarity of this map to our Stokes V map (lower right panel of Figure 6) highlights the potential of using multi-frequency rotation measures (RM) of blazar jets on μas scales to probe where in the jet Faraday conversion is occurring. We have also confirmed (in Figure 10) the sensitivity of CP to the underlying plasma content of the jet (as discussed in Wardle et al. 1998). We intend to compare our synthetic emission maps to upcoming observations that will incorporate phased-ALMA and the orbiting RadioAstron antenna in mm-wave VLBI observations of blazars at 1.3cm ($\sim 20 \mu\text{as}$ resolution). The unprecedented sensitivity and resolution of such observational campaigns will probe where in the jets Faraday conversion is taking place.

The next step to take with this theoretical study is to begin to explore how changes in the TEMZ model parameters affect the levels of circular polarization. These tests will be crucial in assessing the utility of CP measurements in discerning the underlying nature of the jet plasma. The ultimate goal of this research program is the characterization of the lepton content of the jet (f_l). Determining this ratio is vitally important to our understanding of the effect the jet can have on its surrounding environment (“feedback”). By combining maps of m_C and RM, we can observationally constrain the lower limit

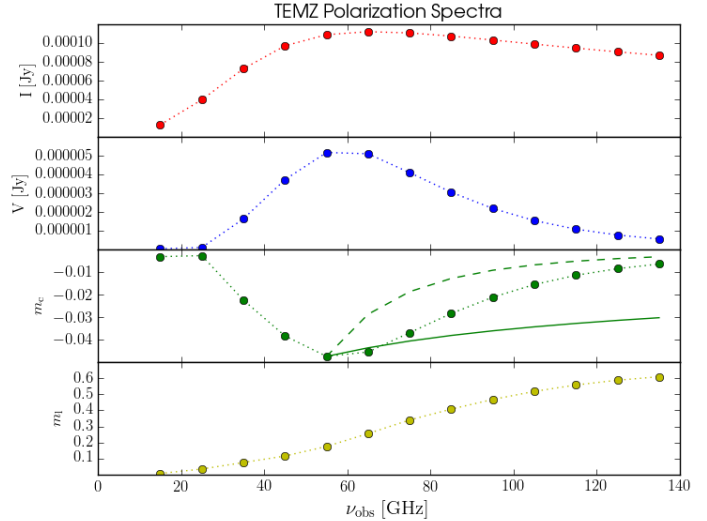


FIG. 11.— Variations of the Stokes parameters as a function of frequency: **(Top panel)** - total intensity, **(Upper middle panel)** - circularly polarized intensity, **(Lower middle panel)** - fractional CP, **(bottom panel)** - fractional LP. The predicted dependences of the intrinsic (green solid) and Faraday conversion (green dashed) mechanisms of CP production as a function of frequency are shown as well.

of the electron power-law energy distribution (γ_{min}) and the parameter $\Lambda (= f_l f_u)$. We plan on compiling a set of simulations that chart a range of plausible plasma compositions (f_l) and jet magnetic field orientations (f_u). Comparison of CP observations with this set of simulations will determine which values of f_l and f_u can match the data, thus probing (in a quantifiable manner) the plasma composition of a relativistic jet.

Finally, our polarized radiative transfer scheme has been written in a robust fashion that will allow it to be used in ray-tracing through other types of numerical jet simulations (for example, particle-in cell (PIC) simulations; Nishikawa et al. 2016, or relativistic-magnetohydrodynamic (RMHD) simulations; Marti et al. 2016). All the routine requires to do so is a three-dimensional distribution of magnetic fields and electron number densities from which full polarization emission maps can be produced.

ACKNOWLEDGEMENTS

Funding for this research was provided by a Canadian NSERC PGS D2 Doctoral Fellowship and by NSF grant AST-1615796. The authors are grateful to S. G. Jorstad, J. L. Gómez, M. Joshi, and J. D. Montgomery for helpful discussions. We have made use of radmc3dPy: a python package/user-interface to the RADMC3D code developed by A. Juhasz.

APPENDIX

A - RADIATIVE TRANSFER OF POLARIZED EMISSION

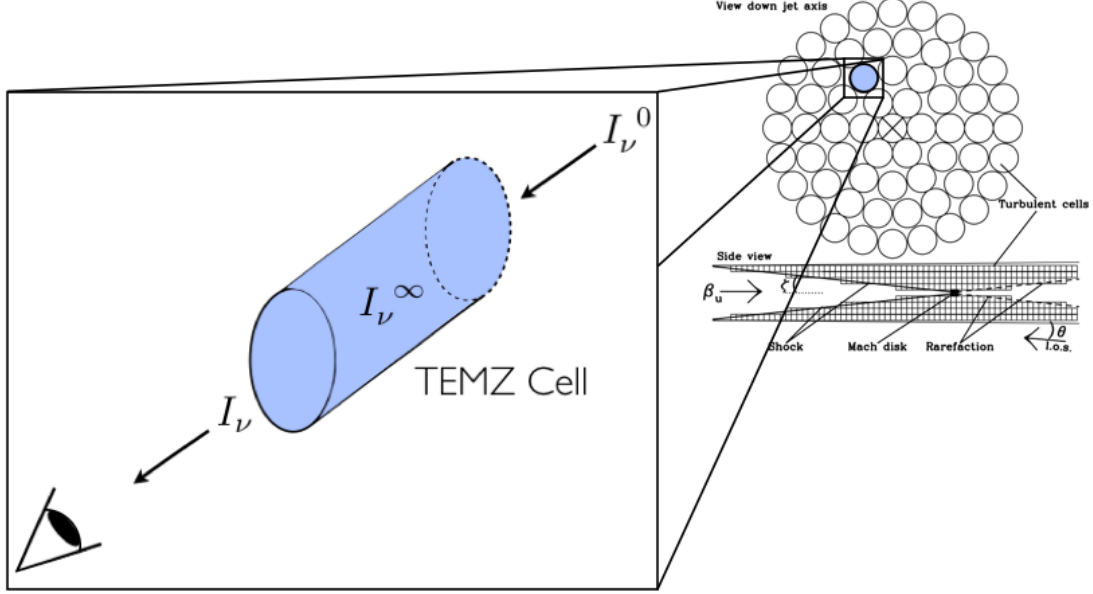


FIG. 12.— Schematic representation of an individual TEMZ cell. Emission from an adjacent cell I_ν^0 enters this cell and combines with the intrinsic cell emission I_ν^∞ to produce the resultant total intensity I_ν that leaves the cell along a given ray.

Stokes I Transfer Function

The full Stokes equations of polarized radiative transfer are presented in Jones & O'Dell (1977). The matrix presented in §3 (Equation 1) can be shown to yield the following expressions for the four Stokes parameters (Equations A1, A17, A18, & A19 below) along a ray passing through a cell of magnetized plasma (see Figure 12). These solutions involve an arbitrary rotation of coordinates to a reference frame in the plasma in which the emission and absorption coefficients of Stokes U are $\eta_\nu^U = \kappa_U = \kappa_U^* = 0$. This rotation, discussed in Jones & O'Dell (1977), makes the mathematics more tractable. In particular, the observed total intensity (I_ν) from a given cell is a “blend” of intrinsic cell emission (I_ν^∞) with external emission (I_ν^0) passing into the cell from an adjacent cell along a particular sight-line:

$$\begin{aligned}
 I_\nu = I_\nu^\infty + e^{-\tau} \left\{ \right. & \cosh(\chi\tau) \left[\frac{1}{2}(1 + q^2 + v^2)(I_\nu^0 - I_\nu^\infty) + (q \times v)(U_\nu^0 - U_\nu^\infty) \right] \\
 & - \sinh(\chi\tau) \left[(q \cdot k)(Q_\nu^0 - Q_\nu^\infty) + (v \cdot k)(V_\nu^0 - V_\nu^\infty) \right] \\
 & + \cos(\chi_*\tau) \left[\frac{1}{2}(1 - q^2 - v^2)(I_\nu^0 - I_\nu^\infty) - (q \times v)(U_\nu^0 - U_\nu^\infty) \right] \\
 & \left. - \sin(\chi_*\tau) \left[(q \times k)(Q_\nu^0 - Q_\nu^\infty) + (v \times k)(V_\nu^0 - V_\nu^\infty) \right] \right\}. \quad (\text{A1})
 \end{aligned}$$

The optical depth of the cell is denoted by τ and is a function of the cell's opacity κ integrated along the ray's path length l through the cell: $\tau = \int \kappa \, dl$. The quantities χ and χ_* , as well as q , v , and k , are defined below and pertain to the effects of Faraday rotation and conversion acting on both the radiation passing through the cell and the radiation intrinsic to the cell. This implies that each cell in the TEMZ computational grid is an “internal” Faraday screen for radiation emanating from adjacent cells along any given sight-line. It is instructive to consider the limiting values of Equation A1. As $\tau \rightarrow \infty$, Equation A1 yields: $I_\nu \rightarrow I_\nu^\infty$. As $\tau \rightarrow 0$, $\sinh(\chi\tau)$ & $\sin(\chi_*\tau) \rightarrow 0$ and $\cosh(\chi\tau)$ & $\cos(\chi_*\tau) \rightarrow 1$. Equation A1 then becomes:

$$I_\nu = I_\nu^\infty + \frac{1}{2}(1 + q^2 + v^2)(I_\nu^0 - I_\nu^\infty) + (q \times v)(U_\nu^0 - U_\nu^\infty) \\ + \frac{1}{2}(1 - q^2 - v^2)(I_\nu^0 - I_\nu^\infty) - (q \times v)(U_\nu^0 - U_\nu^\infty) .$$

Canceling similar terms and rearranging yields:

$$I_\nu = I_\nu^\infty + \frac{1}{2}(I_\nu^0 - I_\nu^\infty)(1 + q^2 + v^2 + 1 - q^2 - v^2) \\ = I_\nu^\infty + \frac{1}{2}(I_\nu^0 - I_\nu^\infty)(2) \\ = I_\nu^\infty + I_\nu^0 - I_\nu^\infty \\ = I_\nu^0 .$$

So, again, as $\tau \rightarrow \infty$, Equation A1 yields: $I_\nu \rightarrow I_\nu^\infty$ (i.e., in the optically thick case the observed intensity is simply equal to the source function intrinsic to the cell), and as $\tau \rightarrow 0$, Equation A1 yields: $I_\nu \rightarrow I_\nu^0$ (i.e., in the optically thin case the observed intensity is simply equal to the unattenuated emission passing through the cell).

Optical Depth

Following Jones & O'Dell (1977) (their equations C4, C6, & C17 for the transfer coefficients of the synchrotron process), the optical depth through a TEMZ cell is evaluated as follows:

$$\tau = \int \kappa \, dl \\ = \int \kappa_\alpha \kappa_\perp (\nu_{B\perp}/\nu)^{\alpha+5/2} \, dl \\ = \int \kappa_\alpha (r_e c) \nu_{B\perp}^{-1} [4\pi g(\vartheta)] [n_0] (\nu_{B\perp}/\nu)^{\alpha+5/2} \, dl \\ = \kappa_\alpha (r_e c) \nu_{B\perp}^{-1} [4\pi g(\vartheta)] [n_0] (\nu_{B\perp}/\nu)^{\alpha+5/2} l , \quad (\text{A2})$$

where l is the path length through the TEMZ cell (evaluated by RADMC3D) and n_0 is the electron number density within the cell; the plasma is homogeneous within each cell. The characteristic length scale of a TEMZ cell for the runs presented here was set to 0.004 pc. The following power-law energy distribution is set in each cell: $n(\gamma) = \int n_o \gamma^{-s} d\gamma$, where the energy of a given electron is $E = \gamma m_e c^2$ and s is a power-law index (related to the optically thin spectral index α by $s = 2\alpha + 1$). This power-law is assumed valid over the energy range γ_{\min} to γ_{\max} , as discussed in §4. The parameter κ_α is a physical constant (of order unity) that is tabulated in Jones & O'Dell (1977) and depends on the value of the spectral index α . The quantity $\nu_{B\perp}$ is given by:

$$\nu_{B\perp} = \frac{eB \sin\vartheta}{2\pi m_e c} , \quad (\text{A3})$$

where ϑ is the angle that the line of sight makes with respect to the local magnetic field vector in the co-moving frame of the plasma cell (see Figure 13).

Relativistic Aberration

When computing ϑ , one needs to account for the effects of relativistic aberration; in particular, the following Lorentz transformation maps our sight-line unit vector \hat{n} in the observer's frame to the corresponding sight-line unit vector \hat{n}' in the co-moving frame of the plasma:

$$\hat{n}' = \frac{\hat{n} + \Gamma \vec{\beta} \left[\frac{\Gamma}{\Gamma+1} \beta \cos(\theta) - 1 \right]}{\Gamma \left[1 - \beta \cos(\theta) \right]} , \quad (\text{A4})$$

(Lyutikov, Pariev, & Gabuzda 2005), where Γ is the bulk Lorentz factor of the jet flow and $\vec{\beta} \equiv \vec{v}_{\text{jet}}/c$. As illustrated in Figure 13, the jet velocity is assumed to be along the \hat{z} -axis and therefore $\vec{\beta} = \{ 0, 0, \beta \}$, where $\beta = \sqrt{1 - \frac{1}{\Gamma^2}}$. From Figure 13 it also follows that: $\hat{n} = \{ \sin(\theta), 0, \cos(\theta) \}$, where θ is the angle of inclination of the jet to the line of sight in the observer's frame. Recalling the definition of the relativistic Doppler boosting factor: $\delta \equiv \frac{1}{\Gamma(1 - \beta \cos(\theta))}$, Equation A4 can be rewritten in component form as:

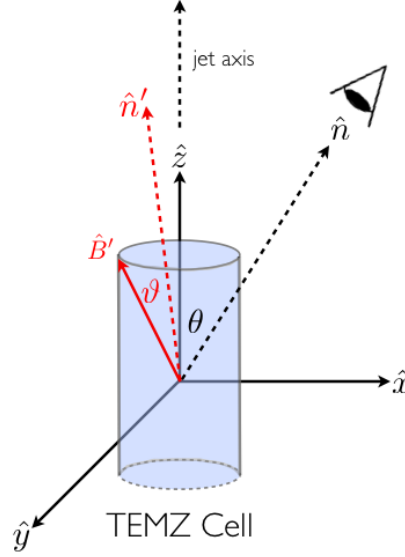


FIG. 13.— A schematic representation of the effect of relativistic aberration on the angle ϑ between the line of sight and the local magnetic field vector within the co-moving frame of the plasma cell. The jet axis is set to \hat{z} and, in the observer's frame, the angle of inclination of the jet to the line of sight is θ . Owing to relativistic aberration, the sight-line is aberrated from \hat{n} to \hat{n}' in the co-moving frame of the plasma. In this figure a prime (in red) denotes the co-moving frame of the plasma.

$$\begin{aligned}\hat{n}' &= \delta \left\{ \sin(\theta), 0, \cos(\theta) + \Gamma\beta \left[\frac{\Gamma}{\Gamma+1} \beta \cos(\theta) - 1 \right] \right\} \\ &= \delta \left\{ \sin(\theta), 0, \Gamma[\cos(\theta) - \beta] \right\},\end{aligned}\quad (\text{A5})$$

after combining terms and simplifying. In the co-moving frame of the plasma, the local magnetic field vector is given by $\hat{B}' = (B_x, B_y, B_z)$. It then follows that:

$$\cos(\vartheta) = \hat{n}' \cdot \hat{B}' \rightarrow \vartheta = \cos^{-1} \left\{ \delta \sin(\theta) B_x + \delta \Gamma[\cos(\theta) - \beta] B_z \right\}. \quad (\text{A6})$$

In Equation A2, the term $g(\vartheta)$ is the pitch angle distribution of the electrons within the plasma. Here we have assumed an isotropic pitch angle distribution, $g(\vartheta) = \frac{1}{2} \sin(\vartheta)$.

Faraday Rotation and Conversion Terms

Returning to Equation A1, χ and χ_* are defined as follows:

$$\chi = \left\| \frac{1}{2} \left\{ \left[(\zeta^2 - \zeta_*^2)^2 + 4(\zeta : \zeta_*)^2 \right]^{\frac{1}{2}} + (\zeta^2 - \zeta_*^2) \right\} \right\|^{\frac{1}{2}} \quad (\text{A7})$$

$$\chi_* = \left\| \frac{1}{2} \left\{ \left[(\zeta_*^2 - \zeta^2)^2 + 4(\zeta_* : \zeta)^2 \right]^{\frac{1}{2}} + (\zeta_*^2 - \zeta^2) \right\} \right\|^{\frac{1}{2}}. \quad (\text{A8})$$

In Equations A7 and A8, ζ and ζ_* represent two-vectors and are defined as follows:

$$\begin{aligned}\zeta &= (\zeta_Q; \zeta_V) \\ \zeta_* &= (\zeta_Q^*; \zeta_V^*),\end{aligned}$$

where (as outlined in Jones & O'Dell 1977) $\zeta : \zeta_* = \zeta_Q \zeta_Q^* + \zeta_V \zeta_V^*$. It also follows that $\zeta^2 = \zeta \cdot \zeta = \zeta_Q^2 + \zeta_V^2$. The expressions ζ_Q , ζ_V , ζ_Q^* , and ζ_V^* are normalized plasma absorption coefficients: $\zeta_{(Q,V)} \equiv \kappa_{(Q,V)}/\kappa_I$; $\zeta_{(Q,V)}^* \equiv \kappa_{(Q,V)}^*/\kappa_I$ (i.e., the κ 's in the matrix shown in §3) and are defined as follows:

$$\zeta_Q = \zeta_\alpha^Q \quad (\text{A9})$$

$$\zeta_V = -\zeta_\alpha^V (\nu_{B\perp}/\nu)^{\frac{1}{2}} \cot(\vartheta) \left[1 + \frac{1}{2\alpha + 3} \right] \quad (\text{A10})$$

$$\zeta_Q^* = -\zeta_\alpha^{*Q} (\nu/\nu_{\min})^{\alpha - \frac{1}{2}} \left\{ \left[1 - \left(\frac{\nu_{\min}}{\nu} \right)^{\alpha - \frac{1}{2}} \right] \left(\alpha - \frac{1}{2} \right)^{-1} \right\} \text{ for } \alpha > \frac{1}{2} \quad (\text{A11})$$

$$\zeta_V^* = \zeta_\alpha^{*V} (\nu/\nu_{\min})^{\alpha + \frac{1}{2}} \frac{\ln \gamma_{\min}}{\gamma_{\min}} \cot(\vartheta) \left[1 + \frac{\alpha + 2}{2\alpha + 3} \right], \quad (\text{A12})$$

where ζ_α^Q , ζ_α^V , ζ_α^{*Q} , and ζ_α^{*V} are physical constants (of order unity) that are tabulated in Jones & O'Dell (1977) and depend on the value of the spectral index α . The quantity $\nu_{\min} \equiv \gamma_{\min}^2 \nu_{B\perp}$. In all of the computations presented in this paper, we have assumed a constant optically thin spectral index of $\alpha = 0.65$ ($s = 2.3$).

In Equation A1, q , v , and k also represent two-vectors and are defined as follows:

$$\begin{aligned} q &= (\zeta_Q, \zeta_Q^*) [\chi^2 + \chi_*^2]^{-\frac{1}{2}} \\ v &= (\zeta_V, \zeta_V^*) [\chi^2 + \chi_*^2]^{-\frac{1}{2}} \\ k &= (\chi, \chi_*) [\chi^2 + \chi_*^2]^{-\frac{1}{2}}. \end{aligned}$$

As outlined in Jones & O'Dell (1977), the dot product (\cdot) and the cross product (\times) operate on q , v , and k in the following manner:

$$q \cdot v = \frac{\zeta_Q \zeta_V + \zeta_Q^* \zeta_V^*}{[\chi^2 + \chi_*^2]},$$

and

$$q \times v = \frac{\zeta_Q \zeta_V^* - \zeta_Q^* \zeta_V}{[\chi^2 + \chi_*^2]}.$$

It also follows that:

$$q^2 = q \cdot q = \frac{\zeta_Q^2 + \zeta_Q^{*2}}{[\chi^2 + \chi_*^2]}.$$

Finally, the quantities pertaining to emission intrinsic to the plasma, I_ν^∞ , Q_ν^∞ , U_ν^∞ , and V_ν^∞ , are defined as follows (see Jones & O'Dell 1977):

$$I_\nu^\infty = \frac{J_\nu}{(1 - \chi^2)(1 + \chi_*^2)} \left\{ [1 + \zeta_*^2] - [\zeta_Q + (\zeta : \zeta_*) \zeta_Q^*] \epsilon_Q - [\zeta_V + (\zeta : \zeta_*) \zeta_V^*] \epsilon_V \right\} \quad (\text{A13})$$

$$Q_\nu^\infty = \frac{J_\nu}{(1 - \chi^2)(1 + \chi_*^2)} \left\{ -[\zeta_Q + (\zeta : \zeta_*) \zeta_Q^*] + [1 + (\zeta_Q^{*2} - \zeta_V^2)] \epsilon_Q + [\zeta_Q \zeta_V + \zeta_Q^* \zeta_V^*] \epsilon_V \right\} \quad (\text{A14})$$

$$U_\nu^\infty = \frac{J_\nu}{(1 - \chi^2)(1 + \chi_*^2)} \left\{ -[\zeta_Q \zeta_V^* - \zeta_Q^* \zeta_V] + [\zeta_V^* - (\zeta : \zeta_*) \zeta_V] \epsilon_Q - [\zeta_Q^* - (\zeta : \zeta_*) \zeta_Q] \epsilon_V \right\} \quad (\text{A15})$$

$$V_\nu^\infty = \frac{J_\nu}{(1 - \chi^2)(1 + \chi_*^2)} \left\{ -[\zeta_V + (\zeta : \zeta_*) \zeta_V^*] + [\zeta_Q \zeta_V + \zeta_Q^* \zeta_V^*] \epsilon_Q + [1 + (\zeta_V^{*2} - \zeta_Q^2)] \epsilon_V \right\}, \quad (\text{A16})$$

where J_ν is the source function of the plasma and ϵ_Q and ϵ_V are Q and V emissivities. For synchrotron emission (see Jones & O'Dell 1977), these three quantities can be shown to be:

$$\begin{aligned} J_\nu &= J_\alpha m_e \nu_{B\perp} \left(\frac{\nu_{B\perp}}{\nu} \right)^{-\frac{5}{2}}, \\ \epsilon_Q &= \epsilon_\alpha^Q, \\ \epsilon_V &= -\epsilon_\alpha^V \left(\frac{\nu_{B\perp}}{\nu} \right)^{\frac{1}{2}} \cot(\vartheta) \left[1 + \frac{1}{2\alpha + 3} \right], \end{aligned}$$

where J_α , ϵ_α , and ϵ_α^V are physical constants (of order unity) that are tabulated in Jones & O'Dell (1977) and depend on the value of the spectral index α .

Stokes Q , U , and V Transfer Functions

The solutions to the other three Stokes parameters (analogous to Equation A1) are given by the following expressions:

$$Q_\nu = Q_\nu^\infty + e^{-\tau} \left\{ \begin{aligned} & \cosh(\chi\tau) \left[\frac{1}{2}(1+q^2-v^2)(Q_\nu^0 - Q_\nu^\infty) + (q \cdot v)(V_\nu^0 - V_\nu^\infty) \right] \\ & - \sinh(\chi\tau) \left[(q \cdot k)(I_\nu^0 - I_\nu^\infty) - (v \times k)(U_\nu^0 - U_\nu^\infty) \right] \\ & + \cos(\chi_*\tau) \left[\frac{1}{2}(1-q^2+v^2)(Q_\nu^0 - Q_\nu^\infty) - (q \cdot v)(V_\nu^0 - V_\nu^\infty) \right] \\ & - \sin(\chi_*\tau) \left[(q \times k)(I_\nu^0 - I_\nu^\infty) + (v \cdot k)(U_\nu^0 - U_\nu^\infty) \right] \end{aligned} \right\} \quad (\text{A17})$$

$$U_\nu = U_\nu^\infty + e^{-\tau} \left\{ \begin{aligned} & \cosh(\chi\tau) \left[-(q \times v)(I_\nu^0 - I_\nu^\infty) + \frac{1}{2}(1-q^2-v^2)(U_\nu^0 - U_\nu^\infty) \right] \\ & - \sinh(\chi\tau) \left[(v \cdot k)(Q_\nu^0 - Q_\nu^\infty) - (q \times k)(V_\nu^0 - V_\nu^\infty) \right] \\ & + \cos(\chi_*\tau) \left[(q \times v)(I_\nu^0 - I_\nu^\infty) + \frac{1}{2}(1+q^2+v^2)(U_\nu^0 - U_\nu^\infty) \right] \\ & - \sin(\chi_*\tau) \left[-(v \cdot k)(Q_\nu^0 - Q_\nu^\infty) + (q \cdot k)(V_\nu^0 - V_\nu^\infty) \right] \end{aligned} \right\} \quad (\text{A18})$$

$$V_\nu = V_\nu^\infty + e^{-\tau} \left\{ \begin{aligned} & \cosh(\chi\tau) \left[(q \cdot v)(Q_\nu^0 - Q_\nu^\infty) + \frac{1}{2}(1-q^2+v^2)(V_\nu^0 - V_\nu^\infty) \right] \\ & - \sinh(\chi\tau) \left[(v \cdot k)(I_\nu^0 - I_\nu^\infty) + (q \times k)(U_\nu^0 - U_\nu^\infty) \right] \\ & + \cos(\chi_*\tau) \left[-(q \cdot v)(Q_\nu^0 - Q_\nu^\infty) + \frac{1}{2}(1+q^2-v^2)(V_\nu^0 - V_\nu^\infty) \right] \\ & - \sin(\chi_*\tau) \left[(v \times k)(I_\nu^0 - I_\nu^\infty) - (q \cdot k)(U_\nu^0 - U_\nu^\infty) \right] \end{aligned} \right\} \quad (\text{A19})$$

Similar to Equation A1, as $\tau \rightarrow \infty$, Equations (A17-A19) yield: $Q_\nu, U_\nu, V_\nu \rightarrow Q_\nu^\infty, U_\nu^\infty, V_\nu^\infty$, respectively (i.e., in the optically thick case the observed intensity of the Stokes parameters is simply equal to the source functions intrinsic to the cell), and as $\tau \rightarrow 0$, Equations (A17-A19) yield: $Q_\nu, U_\nu, V_\nu \rightarrow Q_\nu^0, U_\nu^0, V_\nu^0$ respectively (i.e., in the optically thin case the observed intensity of the Stokes parameters is simply equal to the unattenuated emission passing through the cell.)

Intrinsic Circular Polarization as a Test of the Algorithm

Equations (A1-A19) have been incorporated into a numerical algorithm to solve for I_ν , Q_ν , U_ν , and V_ν along rays passing through the TEMZ grid. This numerical algorithm has been embedded into the ray-tracing code RADMC3D. Each subroutine within this algorithm has been carefully vetted by comparing computed values to analytic calculations. As a further test of this algorithm, we compute the intrinsic fractional circular polarization ($m_c = V/I$) within each cell along a particular sight-line by setting $I_\nu^0 = Q_\nu^0 = U_\nu^0 = V_\nu^0 = 0$ while ray-tracing with RADMC3D. We compare our computed values (Equation A19 divided by A1) to an analytic expression for intrinsic m_c presented in Wardle & Homan (2003):

$$m_c = \frac{V}{I} = \epsilon_\alpha^V \left(\frac{\nu_{B\perp}}{\nu} \right)^{1/2} \cot\vartheta. \quad (\text{A20})$$

The results of this comparison along a random sight-line through the TEMZ grid is illustrated in Figure 14. The excellent agreement between the numerical and analytical calculations implies that Equations (A1-A19) have been incorporated correctly into our numerical algorithm. Figure 14 also illustrates the extreme values of “local” fractional

CP that can be generated within individual TEMZ cells ($m_c \sim 15\%$). The plasma cell where this value is realized possesses, by chance, a local magnetic field vector that is oriented almost along the line of sight in the co-moving frame of the plasma. As discussed in §5, these large values of CP are diluted by smoothing when the resultant image is convolved with a circular Gaussian beam that mimics the resolution of a VLBI array.

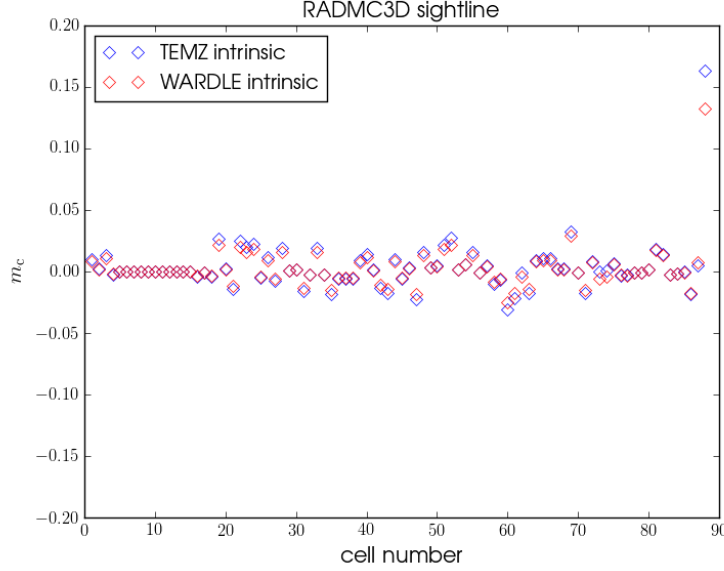


FIG. 14.— Comparison of values of fractional CP ($m_c = V/I$) computed within individual plasma cells of the TEMZ grid along an arbitrarily selected RADMC3D sight-line. The radiative transfer starts at the back of the jet (cell 0) and progresses to the front (cell 90), resulting in the creation of one pixel in our image maps. The red diamonds correspond to values computed with Equation (A20), an analytic expression for m_c taken from Wardle & Homan (2003). The blue diamonds are computed by dividing Equation (A19) by Equation (A1), taken from Jones & O'Dell (1977), where we have set $I_\nu^0 = Q_\nu^0 = U_\nu^0 = V_\nu^0 = 0$ to ensure that the emission is intrinsic. The cell-to-cell agreement between these two quantities along this sight-line represents a successful test of the numerical code. Note also the high value of m_c in the last cell along this particular sight-line.

REFERENCES

- Aharonian, F., Akhperjanian, A. G., Bazer-Bachi, A. R., et al. 2007, *ApJ*, **664**, L71
- Aller, M. F., Aller, H. D., & Hughes, P. A. 2011, *JApA*, **32**, 5
- Aller, H. D., Aller, M. F., & Plotkin, R. M. 2003, *Ap&SS*, **288**, 17
- Cawthorne, T. V., Wardle, J. F. C., Roberts, D. H., & Gabuzda, D. C. 1993, *ApJ*, **416**, 519
- Enßlin, T. A. 2003, *A&A*, **401**, 499
- Gabuzda, D. C., Reichstein, A. R., & O'Neill, E. L. 2013, *arXiv:1410.6653*
- Homan, D. C., Lister, M. L., Aller, H. D., Aller, M. F., & Wardle, J. F. C. 2009, *ApJ*, **696**, 328
- Homan, D. C., Attridge, J. M., & Wardle, J. F. C. 2001, *ApJ*, **556**, 113
- Homan, D. C., & Wardle, J. F. C. 1999, *AJ*, **118**, 1942
- Homan, D. C., & Wardle, J. F. C. 2004, *ApJ*, **602**, L13
- Hughes, P. A., Aller, H. D., & Aller, M. F. 1985, *ApJ*, **298**, 301
- Jones, T. W., & O'Dell, S. L. 1977, *ApJ*, **214**, 522
- Jones, T. W. 1988, *ApJ*, **332**, 678
- Jorstad, S. G., Marscher, A. P., Lister, M. L., et al. 2005, *AJ*, **130**, 1418
- Jorstad, S. G., Marscher, A. P., Stevens, J. A., et al. 2007, *AJ*, **134**, 799
- Jorstad, S. G., Marscher, A. P., Smith, P. S., et al. 2013, *ApJ*, **773**, 147
- Krolik, J. H. 1999, *Active Galactic Nuclei*, Princeton University Press
- Lyutikov, M., Pariev, V. I., & Gabuzda, D. C. 2005, *MNRAS*, **360**, 869
- MacDonald, N. R. 2016, *Galaxies*, **4**, 50
- Marscher, A. P. 2014, *ApJ*, **780**, 87
- Marscher, A. P. 2015, in *Extragalactic Jets from Every Angle*, ed. F. Massaro, C. C. Cheung, E. Lopez, & A. Siemiginowska *IAU Symp.*, **313**, 122
- Marscher, A. P., Jorstad, S. G., Mattox, J. R., & Wehrle, A. E. 2002, *ApJ*, **577**, 85
- Marscher, A. P., Jorstad, S. G., D'Arcangelo, F. D., et al. 2008, *Nature*, **452**, 966
- Marscher, A. P., Jorstad, S. G., Larionov, V. M., et al. 2010, *ApJL*, **710**, 126
- Marscher, A. P., Jorstad, S. G., Agudo, I., MacDonald, N. R., & Scott, T. L. 2012, 2011 Fermi & Jansky: Our Evolving Understanding of AGN
- Martí, J. M., Perucho, M., Gómez, J. L. *ApJ*, in press (2016), *arXiv:1609.00593*
- Nishikawa, K. -I., Hardee, P., Zhang, B., et al. 2013, *Ann. Geophys.*, **31**, 1535
- Nishikawa, K. -I., Frederiksen, J. T., Nordlund, A., et al. 2016, *ApJ*, **820**, 94
- O'Sullivan, S. P., McClure-Griffiths, N. M., Feain, I. J., et al. 2013, *MNRAS*, **435**, 311
- Pacholczyk, A. G. 1970, *Radio Astrophysics*, (San Francisco: Freeman)
- Pushkarev, A. B., Gabuzda, D. C., Vetukhnovskaya, Yu. N., & Yakimov, V. E. 2005, *MNRAS*, **356**, 859
- Ruszkowski, M., & Begelman, M. C. 2002, *ApJ*, **573**, 485
- Smith, P. S. 2016, *Galaxies*, **4**, 27
- Summerlin, E. J., & Baring, M. G. 2012, *ApJ*, **745**, 63
- Wardle, J. F. C., Homan, D. C., Ojha, R., & Roberts, D. H. 1998, *Nature*, **395**, 457
- Wardle, J. F. C., & Homan, D. C. 2003 *Ap&SS*, **288**, 143
- Wehrle, A. E., Grupe, D., Jorstad, S. G., et al. 2016, *ApJ*, **816**, 53

APPENDIX

B - GLOBAL VLBI ARRAY RESOLUTION IMAGES AND SYNCHROTRON OPTICAL, FARADAY ROTATION, AND FARADAY CONVERSION DEPTHS AS A FUNCTION OF FREQUENCY

As discussed in §6, the majority of the synthetic images presented in this paper are of scales within the jet that are smaller than the maximum resolution currently attainable with ground based interferometric arrays. In the interest of making direct comparisons to current (and upcoming) mm-wave VLBI blazar observations, we present in this appendix a series of images identical to those presented in Figures 6 and 7, but that have instead been convolved with a circular Gaussian beam of FWHM $\sim 50 \mu\text{as}$. These images (Figures 15 and 16) mimic the resolution attainable with the longest baselines available to the Global mm VLBI Array (GMVA).

As a further test of our algorithm we picked a sight-line (demarcated with a white cross in the lower right panel of Figure 6) along which we tracked the synchrotron optical depth (τ - Equation A2), the Faraday rotation depth (τ_F - Equation 2), and the Faraday conversion depth (τ_C - Equation 3) through the TEMZ plasma. We did this at frequencies of $\nu_{\text{obs}} = 15, 22$, and 43 GHz. From Equation A2, we know that $\tau \propto \nu^{-(\alpha+5/2)}$. Figure 17 demonstrates that the mean value of the synchrotron optical depth ($\bar{\tau}$) along this sight-line decreases as ν_{obs} increases as expected, and that at $\nu_{\text{obs}} = 43$ GHz the synchrotron emission produced by the TEMZ model is optically thin.

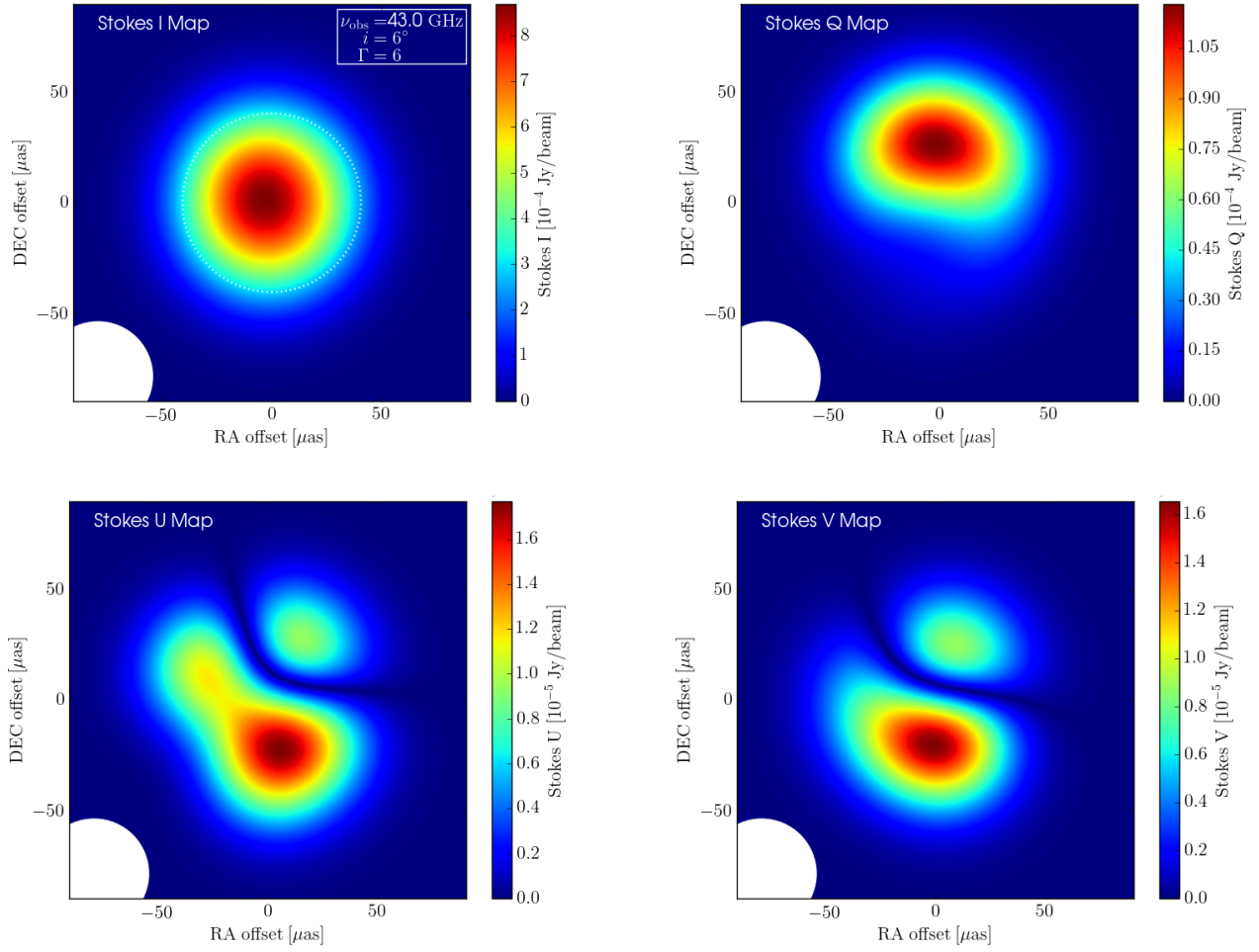


FIG. 15.— **(Upper left panel)** - Total intensity (I) map at an observing frequency of 43 GHz. The white dashed circle defines an arbitrary region within which we compute fractional CP (m_c) and LP (m_l) (presented in Figure 16). **(Upper right panel)** - Q map. **(Lower left panel)** - U map. **(Lower right panel)** - V map. The above images have all been convolved with the circular Gaussian beam of FWHM $\sim 50 \mu\text{as}$ that roughly corresponds to the angular resolution of the longest baselines of a global VLBI array at short radio wavelengths, for comparison with potential future observations. This beam is shown in the lower left of the respective panels.

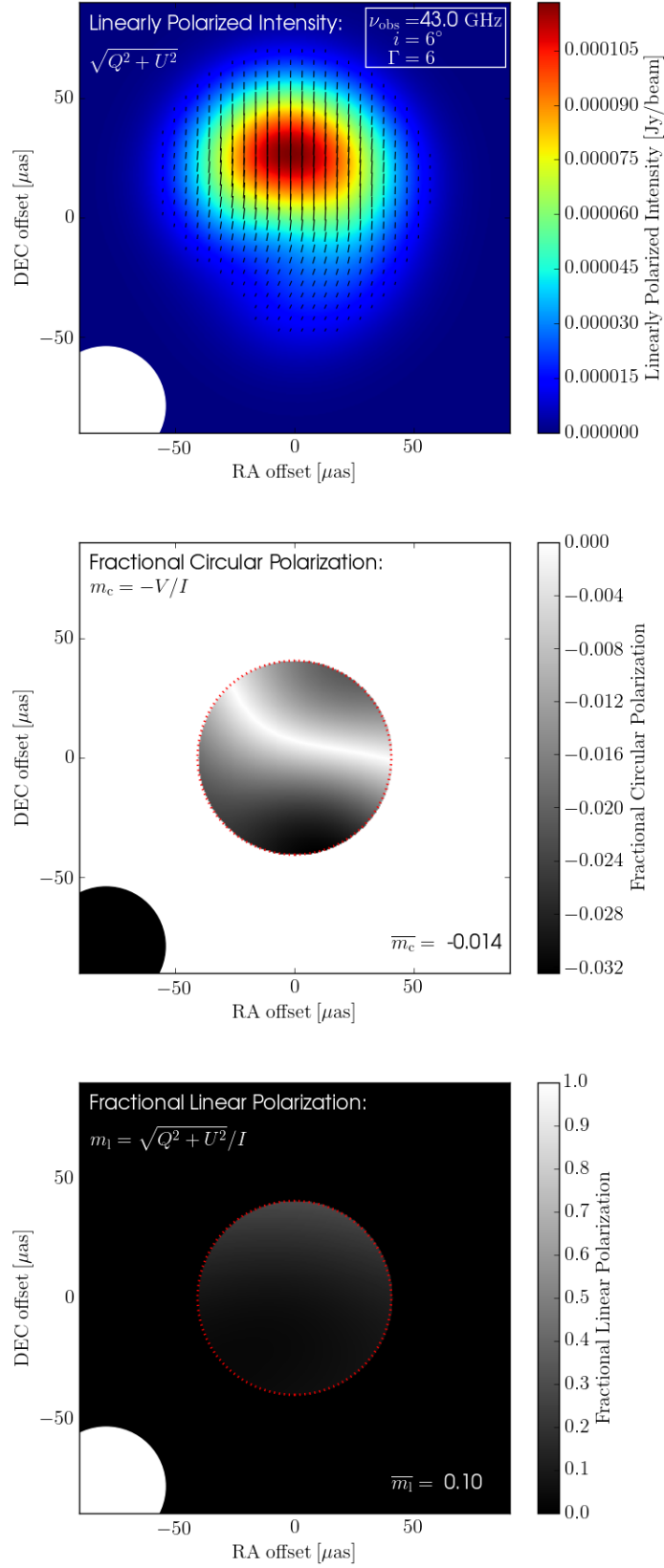


FIG. 16.— **(Upper panel)** - Rendering of linearly polarized intensity P of the disordered TEMZ grid at an observing frequency of 43 GHz. Black line segments indicate the electric vector position angles (EVPAs) as projected onto the plane of the sky. The effects of relativistic aberration (see Lyutikov, Pariev, & Gabuzda 2005) on the orientation of these EVPAs have been included in these calculations. **(Middle panel)** - Map of observed fractional CP, with an integrated value ($\overline{m_c}$) given in the lower right. **(Lower panel)** - Map of observed fractional LP, with an integrated value ($\overline{m_l}$) given in the lower right. The above images have all been convolved with the circular Gaussian beam shown in the lower left of the respective panels.

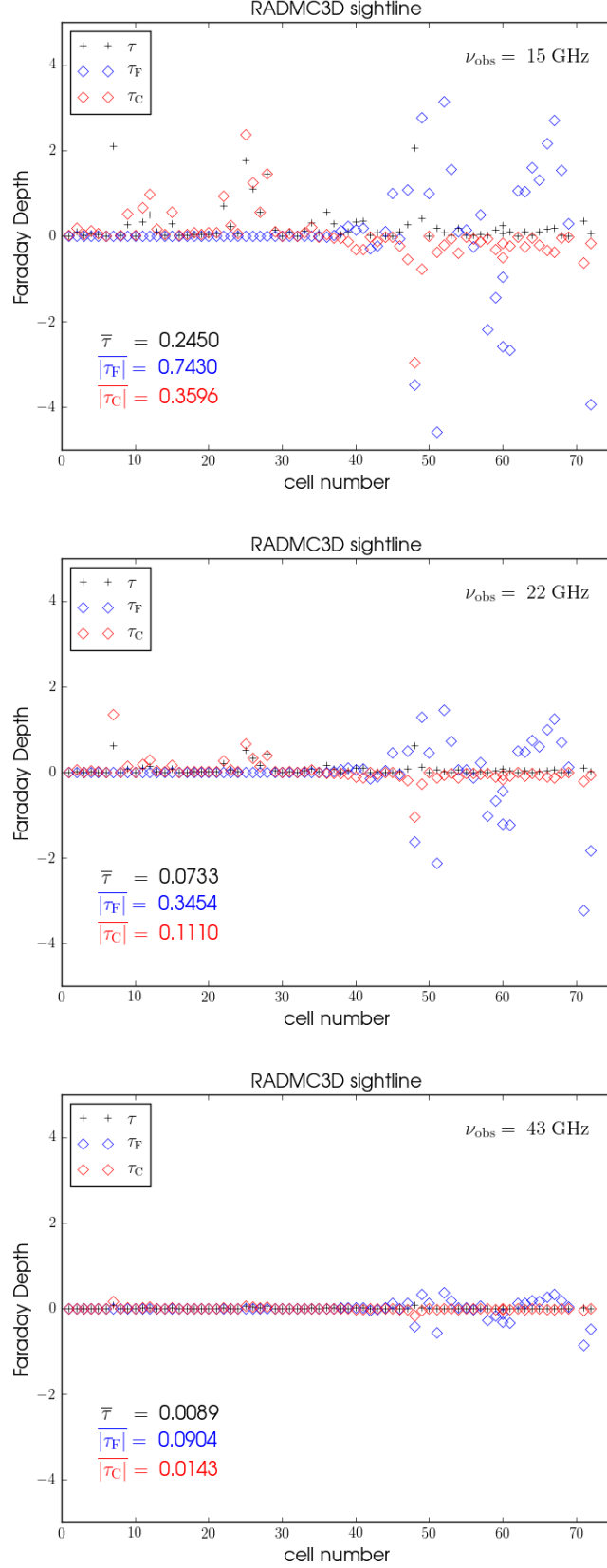


FIG. 17.— **(Upper panel)** - Synchrotron optical depth (τ - Equation A2, black crosses), Faraday rotation depth (τ_F - Equation 2, blue diamonds), and Faraday conversion depth (τ_C - Equation 3, red diamonds) along the sight-line demarcated with a white cross in the lower right panel of Figure 6. The radiative transfer starts at the back of the jet (cell 0) and progresses to the front (cell 70), resulting in the creation of one pixel in our image maps. These values were obtained at an observing frequency of $\nu_{\text{obs}} = 15 \text{ GHz}$. Mean values of the optical, absolute rotation, and absolute conversion depths along this ray are listed in the lower left. **(Middle panel)** - Corresponding values at $\nu_{\text{obs}} = 22 \text{ GHz}$. **(Lower panel)** - Corresponding values at $\nu_{\text{obs}} = 43 \text{ GHz}$.